# "New Cathode Materials for Intermediate Temperature Solid Oxide Fuel Cells"

Final Report

10/1/2003 to 9/30/2006

DE-FC26-03NT41960

December 30, 2006

Allan J Jacobson

Center for Materials Chemistry

University of Houston

Houston, Texas 77204-5003

**Abstract**

Operation of SOFCs at intermediate temperatures (500 – 800 ºC) requires new combinations of electrolyte and electrode materials that will provide both rapid ion transport across the electrolyte and electrode - electrolyte interfaces and efficient electrocatalysis of the oxygen reduction and fuel oxidation reactions. This project concentrates on materials and issues associated with cathode performance that are known to become limiting factors as the operating temperature is reduced.

The specific objectives of the proposed research are to develop cathode materials that meet the electrode performance targets of 1.0 W/cm$^2$ at 0.7 V in combination with YSZ at 700 ºC and with GDC, LSGM or bismuth oxide based electrolytes at 600 ºC. The performance targets imply an area specific resistance of ~0.5 Ωcm$^2$ for the total cell. The research strategy is to investigate both established classes of materials and new candidates as cathodes, to determine fundamental performance parameters such as bulk diffusion, surface reactivity and interfacial transfer, and to couple these parameters to performance in single cell tests.

The initial choices for study were perovskite oxides based on substituted $LaFeO_3$ (P1 compositions), where significant data in single cell tests exist at PNNL for example, for $La_{0.8}Sr_{0.2}FeO_3$ cathodes on both YSZ and CSO/YSZ. The materials selection was then extended to $La_2NiO_4$ compositions (K1 compositions), and then in a longer range task we evaluated the possibility of completely unexplored group of materials that are also perovskite related, the $ABM_2O_{5+\delta}$

A key component of the research strategy was to evaluate for each cathode material composition, the key performance parameters, including ionic and electronic conductivity, surface exchange rates, stability with respect to the specific electrolyte choice, and thermal expansion coefficients. In the initial phase, we did this in parallel with the perovskite compositions that were being investigated at PNNL, in order to assess the relative importance of the intrinsic properties such as oxygen ion diffusion and surface exchange rates as predictors of performance in cell tests. We then used these measurements to select new materials for scaled up synthesis and performance evaluation in single cell tests. The results of the single cell tests than provided feedback to the materials synthesis and selection steps. In this summary, the following studies are reported:

1) Synthesis, characterization, and DC conductivity measurements of the P1 compositions $La_{0.8}Sr_{0.2}FeO_{3-x}$ and $La_{0.7}Sr_{0.3}FeO_{3-x}$ were completed. A combinational approach for preparing a range P1 $(La,Sr)FeO_3$ compositions as thin films was investigated. Synthesis and heat treatment of amorphous $SrFeO_{3-x}$ and $LaFeO_{3-x}$ films prepared by pulsed laser deposition are described.
2) Oxygen transport properties of K1 compositions $La_xPr_{2-x}NiO_{4+d}$ (x =2.0, 1.9, 1.2, 1.0 and 0) measured by electrical conductivity relaxation are presented in this report. Area specific resistances determined by ac impedance measurements for $La_2NiO_{4+\delta}$ and $Pr_2NiO_{4+\delta}$ on CGO are encouraging and suggest that further optimization of the electrode microstructure will enable the target to be reached.

3) The oxygen exchange kinetics of the oxygen deficient double perovskite $LnBaCo_2O_{5.5+\delta}$ (Ln=Pr and Nd) were determined by electrical conductivity relaxation. The high electronic conductivity and rapid diffusion and surface exchange kinetics of PBCO suggest its application as cathode material in intermediate temperature solid oxide fuel cells. The first complete cell measurements were performed on Ni/CGO/CGO/PBCO/CGO cells.

4) The oxygen exchange kinetics of highly epitaxial thin films of $PrBaCo_2O_{5.5+\delta}$ (PBCO) has been determined by electrical conductivity relaxation and isotope exchange and depth profiling and confirm the high electronic conductivity and rapid surface exchange kinetics.

5) The phase compatibility of $La_2NiO_4$, $Pr_2NiO_4$ and $PrBaCo_2O_{5.5+x}$ with YSZ and GDC electrolytes was investigated by solid state reaction and powder X-ray diffraction. PBCO is found to be compatible with CGO.

## 1. Table of Contents


| | | |
|---|---|---|
| | Abstract | 2 |
| 1. | Table of Contents | 4 |
| 2. | Introduction | 8 |
| 3. | Executive Summary | 8 |
| 4. | Experimental & Results | 9 |
| 4.1 | P1 Compositions ($La_{1-x}Sr_xFeO_3$) | 9 |
| 4.1.1 | Synthesis of Perovskite Compositions P1 ($La_{1-x}Sr_xFeO_3$, x = 0.2, 0.3) | 9 |
| 4.1.2 | XPS Analysis and Reaction of $La_{0.7}Sr_{0.3}FeO_3$ | 11 |
| 4.1.3 | DC Conductivity of Perovskite Compositions P1, $La_{1-x}Sr_xFeO_3$, x = 0.2, 0.3 | 11 |
| 4.2 | K1 Compositions ($La_xPr_{2-x}NiO_{4+\delta}$) | 11 |
| 4.2.1 | Synthesis and Characterization of K1 Compositions $La_{1.9}Ce_{0.1}NiO_{4+d}$ and $Pr_{1.9}Ce_{0.1}NiO_{4+d}$ | 11 |
| 4.2.2 | Synthesis of K1 Compositions $La_xPr_{2-x}NiO_{4+d}$ (x =2.0, 1.9, 1.2, 1.0, 0) | 13 |
| 4.2.3 | Characterization of $La_xPr_{2-x}NiO_{4+d}$ (x=2.0, 1.9, 1.2, 1.0, 0) (XRD, TGA) | 13 |
| 4.2.4 | DC Conductivity Measurements | 16 |
| 4.2.5 | Electrical Conductivity Relaxation Measurements | 17 |
| 4.2.6 | Reactions of $La_2NiO_4$ and $Pr_2NiO_4$ with GDC and YSZ | 21 |
| 4.2.7 | Symmetric cell measurements | 22 |
| 4.2.8 | Half cell measurements of PNO and LNO electrodes | 24 |
| 4.3 | P2 compositions $LnBaCo_2O_{5+\delta}$ | 26 |
| 4.3.1 | Synthesis of P2 compositions $LnBaCo_2O_{5+\delta}$ (Ln = Pr and Nd) | 26 |
| 4.3.2 | Characterization of $LnBaCo_2O_{5+\delta}$ (Ln = Pr and Nd) (XRD & TGA) | 27 |
| 4.3.3 | DC Conductivity of $LnBaCo_2O_{5+\delta}$ (Ln = Pr and Nd) | 29 |
| 4.3.4 | ECR Studies of $LnBaCo_2O_{5+\delta}$ (Ln = Pr and Nd) | 29 |
| 4.3.5 | Isotope Exchange and Depth Profiling of $PrBaCo_2O_{5+\delta}$ ceramics. | 31 |
| 4.3.6 | Reactions of $PrBaCo_2O_5$ with GDC and YSZ | 32 |
| 4.3.7 | Impedance Measurements on Symmetric Cells | 33 |
| 4.4 | Solid oxide fuel cells with $PrBaCo_2O_{5+\delta}$ as cathodes | 34 |
| 4.4.1 | fabrication of SOFC with $PrBaCo_2O_{5+\delta}$ as cathodes | 34 |
| 4.4.2 | Electrical measurements | 34 |
| 4.4.3 | Results-voltage-current (V-I) characteristics of SOFCs | 34 |
| 4.5 | Thin films of $PrBaCo_2O_{5+\delta}$ (PBCO) on $SrTiO_3$ (STO) | 35 |
| 4.5.1 | Synthesis of Thin films of $PrBaCo_2O_{5+\delta}$ (PBCO) on $SrTiO_3$ (STO) | 35 |
| 4.5.2 | Characterization of Thin films of $PrBaCo_2O_{5+\delta}$ (PBCO) | 36 |
| 4.4.3 | DC Conductivity of Thin films of $PrBaCo_2O_{5+\delta}$ (PBCO) | 37 |
| 4.4.4 | ECR Studies of Thin films of $PrBaCo_2O_{5+\delta}$ (PBCO) | 37 |
| 4.4.5 | Isotope Exchange and Depth Profiling of Thin Films of $PrBaCo_2O_{5+\delta}$ | 38 |
| 4.4.6 | Additional Isotope Exchange and Depth Profiling of Thin Films of $PrBaCo_2O_{5+\delta}$ (PBCO) | 39 |
| 4.6 | Combinatorial Approach to Measurement of Transport Parameters. | 41 |
| 4.6.1 | Synthesis of Laser Deposition Targets. | 42 |
| 4.6.2 | Deposition and Crystallization of Amorphous Films of $LaFeO_3$ and $SrFeO_{2.5}$ | 42 |

4.6.3 Interdiffusion of Amorphous Bilayer Films of $LaFeO_3$ and $SrFeO_{2.5}$. 43
4.6.4 Surface Analysis of $LaFeO_3$ / $SrFeO_3$ on LAO 44
4.6.5 Laser Deposition of $(La,Sr)FeO_{3-x}$ Samples 45
4.7 Ink jet printing of oxide patterns (University of Toronto) 47
5. Conclusions 47
6. References 48
7. List of Acronyms and Abbreviations 49
8. Publications 49
9. Presentations 50

**List of Tables**

Table 1. Microprobe analysis results for $La_{1-x}Sr_xFeO_3$, x = 0.2 or 0.3. 10
Table 2. Densities of $La_{1-x}Sr_xFeO_3$, x = 0.2, 0.3 samples. 10
Table 3. Summary of the thermodynamic factors for $LnBaCo_2O_{5+\delta}$ (Ln = Pr, Nd). 26
Table 4. Thin film samples and annealing conditions. 46

**List of Graphical Materials**

Figure 1. XRD powder pattern and backscattered electron image of $La_{0.8}Sr_{0.2}FeO_3$, prepared via solid-state synthesis. 10
Figure 2. Photoelectron spectra of the as received $La_{0.7}Sr_{0.3}FeO_3$ sample (prepared via the solid-state method) and of the cleaned $La_{0.7}Sr_{0.3}FeO_3$ pellet. 11
Figure 3. DC conductivity of $La_{1-x}Sr_xFeO_3$, x = 0.2, 0.3 in 100% oxygen. 12
Figure 4. X-ray Powder Diffraction Data for $La_{1.9}Ce_{0.1}NiO_{4+\delta}$ and $Pr_{1.9}Ce_{0.1}NiO_{4+\delta}$. 12
Figure 5. X-ray Powder Diffraction Data for $La_2NiO_{4+\delta}$ and $Pr_2NiO_{4+\delta}$ 13
Figure 6. Electron Probe Microanalysis Results for $La_2NiO_{4+\delta}$. Analysis points were selected randomly. 14
Figure 7. Cell parameters a, b and c (Å) versus x in $La_xPr_{2-x}NiO_{4+\delta}$. 14
Figure 8. Thermogravimetic analysis data for $La_xPr_{2-x}NiO_{4+}$□ (a): $La_2NiO_{4+\delta}$, (b): $Pr_2NiO_{4+\delta}$; (c):x = 1.9, (d): x = 1.2, (e) x = 1.0. 15
Figure 9. The total conductivity of $La_2NiO_{4+\delta}$ (left) and $Pr_2NiO_{4+\delta}$ (right) 16
Figure 10. Conductivity data for $La_xPr_{2-x}NiO_{4+\delta}$ (x = 1.9, 1.2 and 1) at 10 % and 1 % $pO_2$. 17
Figure 11. Comparison of the DC conductivities for $La_xPr_{2-x}NiO_{4+\delta}$ vs. temperature and vs composition at 1000/T = 2.0. 17
Figure 12. Typical conductivity relaxation data for $La_2NiO_{4+\delta}$ 18
Figure 13. Values of $D_{chem}$ (left) and $D_O$ (right) determined by Electrical Conductivity Relaxation. 19
Figure 14. Comparison of the present results with the IEDP data of reference 3 and 11. 19

| | | |
|---|---|---|
| Figure 15. | Values of $D_{chem}$(left) and $k_{chem}$(right) of $La_xPr_{2-x}NiO_{4+\delta}$ (x = 1.9, 1.2, 1). | 20 |
| Figure 16. | Values of $D_o$ (left) and $k_{ex}$ (right) at 3 % $pO_2$ except 0.5 % for $La_{1.9}Pr_{0.1}NiO_{4+\delta}$ determined by electrical conductivity relaxation. | 20 |
| Figure 17. | X-ray data for a LNO/YSZ mixture after heat treatment at 1075 °C | 21 |
| Figure 18. | X-ray diffraction patterns of mixtures of LNO-CGO and PNO-CGO after heat treatments. | 21 |
| Figure 19. | Representative impedance spectra of the $Pr_2NiO_{4+\delta}$ electrochemical cell: $Pr_2NiO_{4+\delta}$ /CGO/ $Pr_2NiO_{4+\delta}$ (T= 527 °C). | 22 |
| Figure 20. | Area Specific Resistance vs. Temperature for $La_2NiO_{4+\delta}$ and $Pr_2NiO_{4+\delta}$ | 23 |
| Figure 21. | The variation of the ASR with oxygen partial pressure at different temperatures. | 23 |
| Figure 22. | A comparison of measurements of the electrode resistance of LNO and PNO at $pO_2$ = 0.21 atm (left) and 1 atm (right). | 25 |
| Figure 23. | Cyclic voltammetry measurements for LNO and PNO at 650 °C showing the large difference in performance. | 25 |
| Figure 24. | The structure of $LnBaCo_2O_{5+\delta}$; the purple and silver spheres represent the barium and lanthanide cations, the square pyramidal coordination of cobalt ions is shown in blue, and the partially occupied oxygen ion sites as orange spheres. | 26 |
| Figure 25. | Rietveld refinement of $PrBaCo_2O_{5.7}$ | 27 |
| Figure 26. | Thermogravimetric analysis of $LnBaCo_2O_{5+\delta}$ (Ln = Pr, Nd). | 27 |
| Figure 27. | The thermodynamic factors for $LnBaCo_2O_{5+\delta}$ (Ln = Pr, Nd). | 28 |
| Figure 28. | Total conductivity of $LnBaCo_2O_{5+\square}$, (Ln=Pr, Nd).The open and closed symbols correspond to measurements on increasing and decreasing temperature. | 29 |
| Figure 29. | $D_{chem}$ and $k_{chem}$ obtained for $LnBaCo_2O_{5+\delta}$(Ln = Pr, Nd). | 30 |
| Figure 30. | The temperature dependence of the self-diffusion ($D_O^{2-}$) and surface exchange coefficients ($k_{ex}$) for $LnBaCo_2O_{5.5+\delta}$ (Ln = Pr, Nd). | 30 |
| Figure 31. | IEDP results for $PrBaCo_2O_{5+\delta}$ infused at 4000C for 5 min in 0.2 atm $^{18}O_2$ (99%). a: secondary electron image with $PrBaCo_2O_{5.5+\delta}$ region on the right and epoxy matrix on left. b SIMS image of the fraction of $^{18}O$, $f^{18}O = (^{18}O/(^{18}O+^{16}O))$ of the same region as in panel a. c: the profile of $f^{18}O$ derived from the image in panel b. | 31 |
| Figure 32. | Comparison of the values of $D_O$ and of $k_O$ measured by ECR for ceramic samples. | 32 |
| Figure 33. | An X-ray diffraction patterns of 75-25 PBCO/CGO composite sintered at 1050 °C, * indicates CGO. | 32 |
| Figure 34. | Area Specific Resistances for three symmetric cells. PBCO/CGO/PBCO. | 33 |
| Figure 35. | V-I characteristics and power densities of the cell as a function of current densityof the CGO electrolyte supported solid oxide fuel cell with a PBCO cathode. | 35 |
| Figure 36. | Open circuit voltages (left) and a comparison of the ohmic resistance | 35 |

of the cell measured by current interrupt technique and the calculated theoretical resistance of the electrolyte.
Figure 37. Grazing incidence diffraction scans along the substrate's [200] direction for different scattering depths. The curves are shifted for clarity. Labeling of the PBCO peaks is according to the Pmmm structure. The asterisk marks an (unknown) interfacial phase. 36
Figure 38. Conductivity of a PBCO film in air. Solid and open symbols correspond to measurements made on increasing and decreasing temperature, respectively. 37
Figure 39. Representative conductivity relaxation data for PBCO/STO at 430 ºC. The gas switch was from 5% to 1% $O_2$. $A_1 = 0.48$, $A_2 = 0.49$, $\tau_1 = 34.5$ s, $\tau_2 = 284$ s. The error axis indicates differences between the experimental data and the fit. 38
Figure 40. The surface exchange coefficients measured for PBCO/STO. The filled symbols correspond to a gas switch from 0.02 to 0.1 atm and the open symbols from 0.1 to 0.02 atm. The cross hatched square is the IEDP measurement. 39
Figure 41. Depth Profile of PBCO/YSZ. 40
Figure 42. Depth Profile of PBCO/CGO/YSZ. 40
Figure 43. Comparison of the IEDP and ECR measurements of the surface exchange coefficients of PBCO films. 41
Figure 44. Schematic of the approach to make multiple compositions on one Substrate. 41
Figure 45. Temperature dependence of the resistance of amorphous $SrFeO_{2.5}$ and $LaFeO_3$ films. 43
Figure 46. XRD patterns of annealed thin films on LAO substrate, a) $SrFeO_3/LaFeO_3$ b) $LaFeO_3/SrFeO_3$, after heated in $O_2$ at 380 °C for 110 h and followed by 715 °C for 8 h. 44
Figure 47. $Ga^+$ SIMS depth profile of $LaFeO_3$ on $SrFeO_3$ on a LAO substrate. 45
Figure 48. XRD pattern of an annealed 4-layer Sr/La/Sr/La thin film after heating in air at 500 °C 113 h and then 700 °C for 10 h. 46

## 2. Introduction

The objectives of the project are to discover new oxide cathode materials that meet a performance target of 1.0 W/cm$^2$ at 0.7 V in combination with YSZ at 700 ºC and with CGO, LSGM electrolytes at 600 ºC. An ancillary objective of the project is to increase fundamental understanding of the intrinsic transport properties of mixed electronic ionic conducting oxides and oxide-oxide interfaces that can be used to accelerate further progress in the development of cost effective high performance solid oxide fuel cells. In Phase I, we measured the surface exchange rates, diffusion coefficients and interfacial transport for an initial set of perovskite related oxide materials (K1 compositions). In Phase II we synthesized and characterized new cathode materials (P1 and P2 compositions) and measured their kinetic parameters. The chemical compatibility with different electrolytes was determined. Based on the results, a subset of the best materials was selected for single cell tests. The phase III objective was to evaluate the performance of the best materials identified in Phase I and II.

## 3. Executive Summary

The project began on October 1, 2003 and this is the final report on the work that has been completed.

We have prepared thin oxide films by pulsed laser deposition for study of transport kinetics. We adopted a combinatorial approach, initially with the $LaFeO_3$ – $SrFeO_{2.5}$ system for study of transport kinetics. Thin film samples of both compositions have been made in amorphous form and the crystallization behavior determined. Two layer thin films of $LaFeO_3$ and $SrFeO_{2.5}$ have been prepared by PLD in amorphous form and their inter-diffusion investigated at different temperatures studied. We have also synthesized and measured the DC conductivity of two examples of P1 compositions $La_{0.7}Sr_{0.3}FeO_3$ and $La_{0.8}Sr_{0.2}FeO_3$ and characterized the surface chemistry. With PNNL, we extended the P1compositions to include copper substituted samples.

We have prepared single phase samples of $Ln_2NiO_4$ series,[1-9] $La_xPr_{2-x}NiO_{4+d}$ (x =2.0, 1.9, 1.5, 1.2, 1.0, 0.5 and 0), and characterized them by X-ray powder diffraction. We have measured the dc conductivities as a function of $pO_2$ in several oxygen partial pressures and made electrical conductivity relaxation measurements as function of temperature for several different $pO_2$ switches. Thermogravimetric analysis measurements were completed and the oxygen ion diffusion coefficients and the surface exchange coefficients extracted for comparison with previous measurements. We have evaluated the performance of $Ln_2NiO_{4+\delta}$, Ln =La, Pr, in symmetric cells. Reactivity studies indicated evidence for significant reaction with YSZ and so the data were collected on gadolinium doped ceria electrolytes. The area specific resistances are low enough to warrant further studies. Samples (10 g) were sent to PNNL for further evaluation.

The oxygen exchange kinetics of the oxygen deficient double perovskite $LnBaCo_2O_{5.5+x}$ (Ln = Pr and Nd) have been determined by electrical conductivity relaxation. $LnBaCo_2O_{5.5+\delta}$ (Ln = Pr and Nd) were prepared by citric precursor method. An improved densification process for PBCO has been developed. Using samples prepared by this method, the total DC conductivity is found to reach 2000 Scm$^{-1}$. The chemical oxygen diffusion coefficient ($D_{chem}$) and the surface exchange coefficient ($k_{chem}$) obtained by ECR were converted into the tracer diffusion coefficient ($D_{O^{2-}}$) and surface exchange

coefficient ($k_{ex}$) with thermodynamic factors measured by TGA, in order to compare with the values obtained by isotope exchange and depth profiling. The high electronic conductivity and rapid diffusion and surface exchange kinetics of $PrBaCo_2O_{5.5+x}$ suggest its application as cathode material in intermediate temperature solid oxide fuel cells. Preliminary measurements show low ASR values at 600 °C. These results led to extended measurements on complete cells and we describe here the results that we have obtained for electrolyte supported cells.

The oxygen exchange kinetics of highly epitaxial thin films of the oxygen deficient double perovskite $PrBaCo_2O_{5.5+\delta}$ (PBCO) have been determined by electrical conductivity relaxation and isotope exchange and depth profiling. The thin films of $PrBaCo_2O_{5.5+\delta}$ were prepared by pulsed laser deposition (PLD) on single crystal substrates. The electrical conductivity relaxation (ECR) and isotope measurements agree well though the ECR data indicate the presence of two distinct kinetic pathways. Isotope exchange and depth profiling of thin film structures on both YSZ and CGO show little or no barrier to interfacial transport. The high electronic conductivity and rapid surface exchange kinetics of PBCO film are consistent with the results for bulk materials.

A commercial piezo-electric ink-jet printer was been modified to deposit patterned oxide layers on single crystal and ceramic substrates. Preliminary patterns were generated to test the roles of surfaces and phase boundaries (double and triple) in the activation and transport of oxygen by isotope methods.

We have also investigated the possibility of substituting cerium for either lanthanum or praseodymium in 214 systems. This was not successful and even at small doping levels a second fluorite phase is apparent. This suggests that these materials will be compatible with CGO. The phase compatibility of $La_2NiO_4$, $Pr_2NiO_4$ and $PrBaCo_2O_{5.5+x}$ with YSZ and GDC electrolytes was investigated by solid state reaction and powder X-ray diffraction. PBCO is found to be compatible with CGO.

## 4. Experimental & Results

### 4.1 P1 Compositions ($La_{1-x}Sr_xFeO_3$)

#### 4.1.1 Synthesis of Perovskite Compositions P1 ($La_{1-x}Sr_xFeO_3$, x = 0.2, 0.3)

The glycine-nitrate and solid-state methods were used to synthesize $La_{0.7}Sr_{0.3}FeO_3$ and $La_{0.8}Sr_{0.2}FeO_3$ (LSFO). $La_2O_3$ (Aldrich 99.9%), $SrCO_3$ (Aldrich 99.9%), and $Fe_2O_3$ (Aldrich 99.9%) were used in the solid-state synthesis method. Iron metal (Aldrich (99.99%) is used in place of $Fe_2O_3$ in the glycine-nitrate synthesis method. $La_2O_3$ was dried at 1000 ºC, Fe, $Fe_2O_3$, and $SrCO_3$ are dried at 125 ºC. All reagents are dried for 16 h. Stoichiometric quantities were then used for synthesis.

After ignition in the glycine-nitrate process and subsequent grinding, the compositions were heated at 1000 ºC. The samples were then ground and reheated at 1200, 1250, and 1300 ºC. Phase pure and homogeneous samples were obtained except $La_{0.8}Sr_{0.2}FeO_3$, prepared via the glycine-nitrate method. A representative X-ray powder pattern and backscattered electron image is shown in Figure 1. The stoichiometries determined by microprobe analysis and the densities measured by the Archimedes method are given in Table 1 and Table 2. The analytical data $La_{0.8}Sr_{0.2}FeO_3$, prepared via the glycine-nitrate

method show significant variations in the La and Sr compositions at different points on the sample indicating poor homogeneity. This sample will not be considered further.

Table 1. Microprobe analysis results for $La_{1-x}Sr_xFeO_3$, x = 0.2 or 0.3

| | I | II | III | IV | V | average | range |
|---|---|---|---|---|---|---|---|
| **$La_{0.8}Sr_{0.2}FeO_3$ glycine-nitrate** | | | | | | | |
| **La** | 0.89 | 0.81 | 0.84 | 0.88 | 0.80 | 0.85 | 0.09 |
| **Sr** | 0.11 | 0.19 | 0.16 | 0.12 | 0.20 | 0.15 | 0.09 |
| **Fe** | 1.12 | 1.05 | 1.02 | 1.12 | 1.08 | 1.08 | 0.10 |
| **$La_{0.8}Sr_{0.2}FeO_3$ solid-state** | | | | | | | |
| **La** | 0.79 | 0.80 | 0.80 | 0.79 | 0.79 | 0.79 | 0.02 |
| **Sr** | 0.21 | 0.20 | 0.20 | 0.21 | 0.21 | 0.21 | 0.02 |
| **Fe** | 1.06 | 1.08 | 1.09 | 1.07 | 1.08 | 1.08 | 0.02 |
| **$La_{0.7}Sr_{0.3}FeO_3$ glycine-nitrate** | | | | | | | |
| **La** | 0.71 | 0.71 | 0.70 | 0.71 | 0.70 | 0.71 | 0.01 |
| **Sr** | 0.29 | 0.29 | 0.30 | 0.29 | 0.30 | 0.29 | 0.01 |
| **Fe** | 1.09 | 1.09 | 1.06 | 1.10 | 1.07 | 1.08 | 0.03 |
| **$La_{0.7}Sr_{0.3}FeO_3$ solid-state** | | | | | | | |
| **La** | 0.71 | 0.69 | 0.69 | 0.69 | 0.70 | 0.70 | 0.02 |
| **Sr** | 0.29 | 0.31 | 0.31 | 0.31 | 0.30 | 0.30 | 0.02 |
| **Fe** | 1.10 | 1.06 | 1.07 | 1.07 | 1.08 | 1.08 | 0.04 |

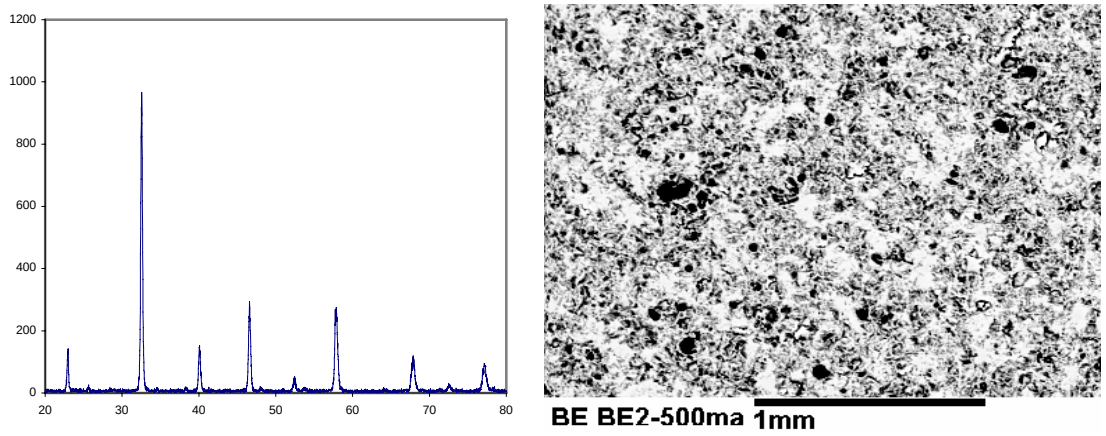


Figure 1. XRD powder pattern and backscattered electron image of $La_{0.8}Sr_{0.2}FeO_3$, prepared via solid-state synthesis.

Table 2. Densities of $La_{1-x}Sr_xFeO_3$, x = 0.2, 0.3 samples

| | **$La_{0.8}Sr_{0.2}FeO_3$** | | **$La_{0.7}Sr_{0.3}FeO_3$** | |
|---|---|---|---|---|
| | glycine-nitrate | solid-state | glycine-nitrate | solid-state |
| d g/cm$^3$ | 5.80 | 6.11 | 5.96 | 5.93 |
| % Theoretical | 88.3 | 93.1 | 92.5 | 91.6 |

### 4.1.2 XPS Analysis and Reaction of $La_{0.7}Sr_{0.3}FeO_3$

The sintered pellet of $La_{0.7}Sr_{0.3}FeO_3$, synthesized by the solid-state method, was analyzed by X-ray photoelectron spectroscopy (XPS) to characterize the surface composition. XPS analysis was performed at both 70º and 15º take-off angles. The 15º angle is used to probe the near surface region while the 70º angle data give information at greater depth. Combined, the data at the two angles reveal which binding energies correspond to lattice oxygen or surface oxides. The results are shown in Figure 2. The higher binding energies from 530 to 533 eV correspond to surface oxides and the lower binding energy of 528.5 eV corresponds to lattice oxygen. The very large peak height at the higher binding energies indicates that the surface is highly contaminated with carbonates.

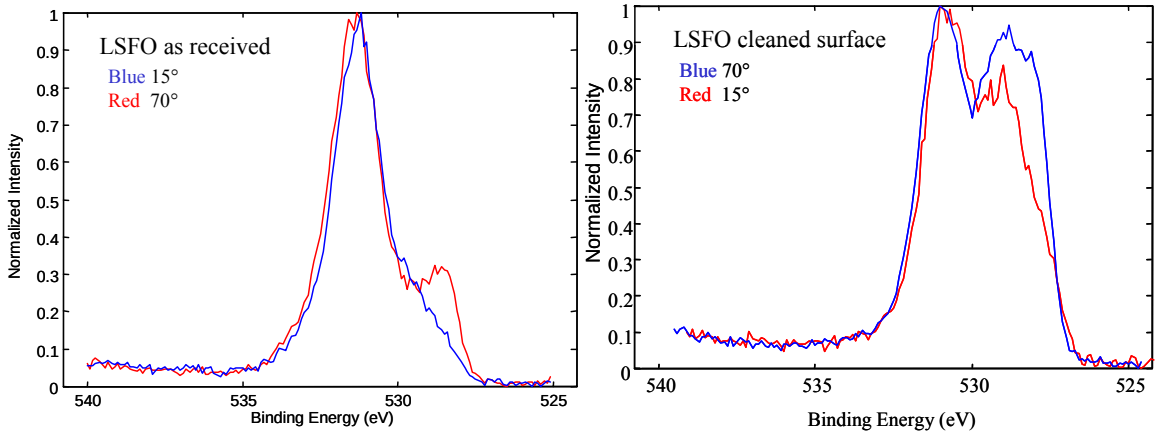


Figure 2. Photoelectron spectra of the as received $La_{0.7}Sr_{0.3}FeO_3$ sample (prepared via the solid-state method) (left) and of the cleaned $La_{0.7}Sr_{0.3}FeO_3$ pellet (right).

The sample was then transferred from the XPS chamber to an attached reaction chamber where it was heated in 100% $O_2$ at 350 ºC for 1.5 h to remove surface contaminants. The sample was cooled to room temperature and transferred back to the XPS chamber for subsequent analysis. XPS data were measured at both angles and confirm that the surface carbonates have been removed.

### 4.1.3 DC Conductivity of Perovskite Compositions P1, $La_{1-x}Sr_xFeO_3$, x = 0.2, 0.3

Pressed pellets of the four compounds were sintered and cut into bars for DC conductivity measurements using the procedure described previously. The results (Figure 3) are similar to other perovskite systems. The conductivity on increasing temperature shows Arrhenius behavior followed by a decrease as oxygen is lost from the sample on heating. The conductivity at x = 0.3 is somewhat higher than at x = 0.2.

## 4.2 K1 Compositions ($La_xPr_{2-x}NiO_{4+d}$)

### 4.2.1 Synthesis and Characterization of K1 Compositions $La_{1.9}Ce_{0.1}NiO_{4+d}$ and $Pr_{1.9}Ce_{0.1}NiO_{4+d}$

The syntheses of $La_{1.9}Ce_{0.1}NiO_{4+d}$ and $Pr_{1.9}Ce_{0.1}NiO_{4+d}$ were attempted by using a solid-state reaction method. The samples were sintered at 1350 °C for 24 h in air with constant heating and cooling rates of 2°C /min). Samples were reground once between firings.

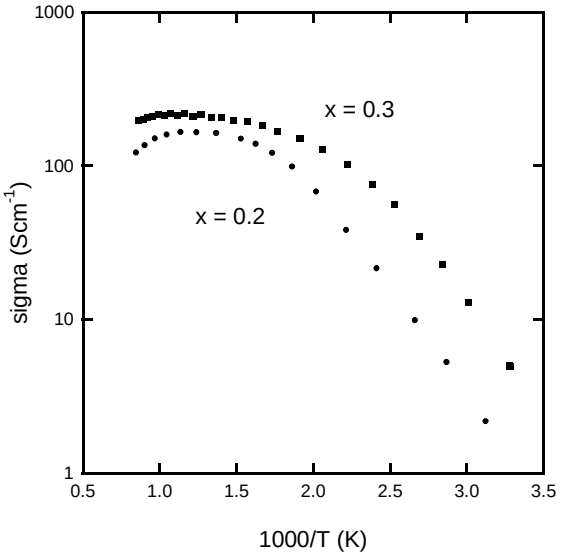


Figure 3. DC conductivity of $La_{1-x}Sr_xFeO_3$, x = 0.2, 0.3 in 100% oxygen.

We were unable to synthesize $La_{1.9}Ce_{0.1}NiO_{4+x}$ and $Pr_{1.9}Ce_{0.1}NiO_{4+x}$. X-ray powder patterns (Figure 4) always show the presence of extra lines which are identified as coming from $CeO_2$ with the fluorite structure, possibly substituted with some nickel. The failure to form a solid solution under these condition is most likely due to the stability of $Ce^{4+}$ which, with a radius $r$ = 0.87 Å, is too small to occupy either $La^{3+}$ sites ($r$ = 1.16 Å) or $Pr^{3+}$ ($r$ = 1.26 Å) sites.

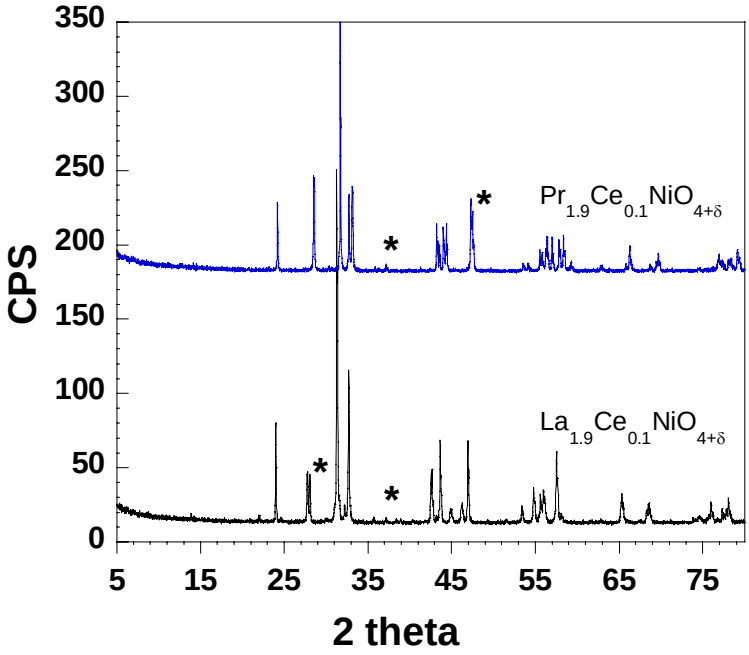


Figure 4. X-ray Powder Diffraction Data for $La_{1.9}Ce_{0.1}NiO_{4+x}$ and $Pr_{1.9}Ce_{0.1}NiO_{4+x}$.

### 4.2.2 Synthesis of K1 Compositions $La_xPr_{2-x}NiO_{4+d}$ (x =2.0, 1.9, 1.2, 1.0 and 0)

Samples of $La_xPr_{2-x}NiO_{4+d}$ compounds were synthesized via a citrate precursor method. Stoichiometric amounts of $La_2O_3$ (Alfa 99.99+ %) and $Pr_6O_{11}$ (Aldrich 99.9%) preheated previously at 1000 °C in air to remove absorbed water and carbonate, and NiO (0.03 mol Aldrich, 99.99 %), also preheated at 600 °C in air were dissolved in 3M nitric acid. Ethylene glycol (13 ml, EM science >98 %) and citric acid (17 g, Aldrich, 99.5 %) were added to stabilize the solutions. This mixture was covered and stirred at 150 °C until the solution began to foam and formed a dry resin. The dry foam containing residual organic components was decomposed by further heating at 300 °C and then at 600 °C for 24 h periods. The final mixture was pressed with a load of 5 tons into a 1-inch diameter die. The pellets were sintered in air at 1350 °C for 24 h with a constant heating and cooling rate (2 °C/min.). In the case of $Pr_2NiO_{4+d}$, the sample was reground once between firings.

### 4.2.3 Characterization of $La_xPr_{2-x}NiO_{4+d}$ (x =2.0, 1.9, 1.2, 1.0 and 0) (XRD & TGA)

X-ray powder diffraction measurements (Scintag XDS 2000) with Cu Kα radiation were performed to identify the structures. A scan rate of 0.125°/min was used with the range $5° \leq 2\theta \leq 80°$. Lattice parameters were obtained from the indexed powder patterns by using the program PowderCell 2.4. Both the $La_2NiO_{4+x}$ and $Pr_2NiO_{4+x}$ samples are single phase by X-ray powder diffraction and can be indexed with a tetragonal unit cell for $La_2NiO_{4+x}$ (a = 3.861(1) Å, c = 12.666(2) Å) and an orthorhombic unit cell for $Pr_2NiO_{4+x}$ (a = 5.4523(2) Å, b = 5.3962(3) Å and c = 12.4314(3) Å). The data are shown in Figure 5.

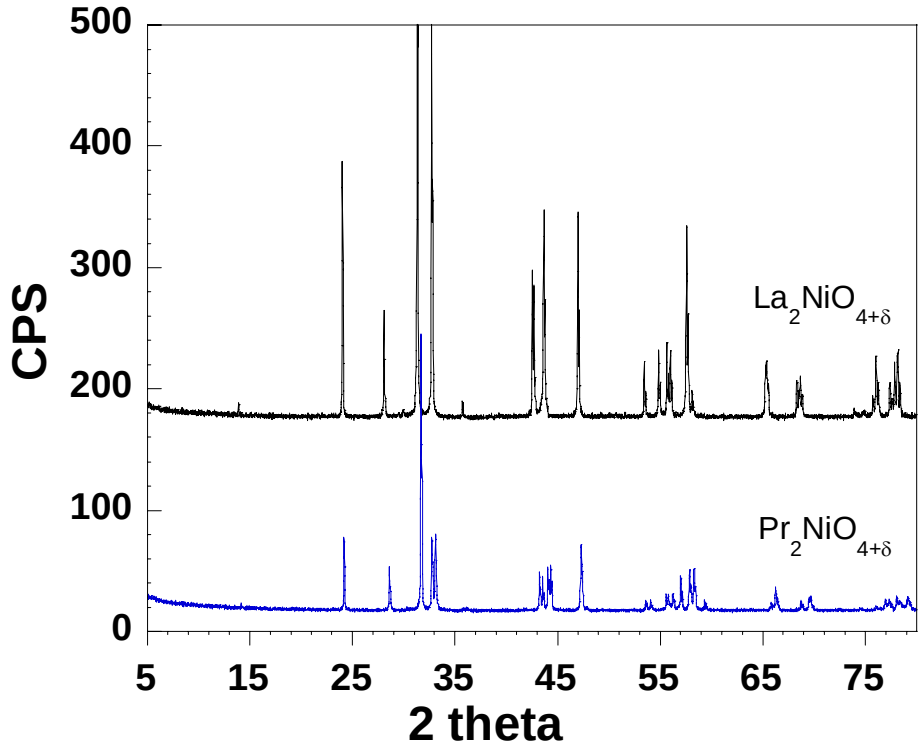


Figure 5. X-ray Powder Diffraction Data for $La_2NiO_{4+x}$ and $Pr_2NiO_{4+x}$

The phase purity of the $La_2NiO_{4+d}$ sample also was determined using Electron Microprobe Analysis (EPMA) with a JEOL JXA 8600 electron microprobe. Electron microprobe analysis for $La_2NiO_4$ shows that the sample is homogeneous in composition apart from a trace amount of $La_2O_3$ (see Figure 6).

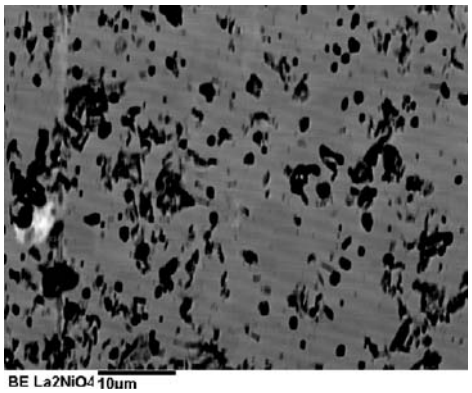


| point # | Atomic % | | |
|---|---|---|---|
| | La | Ni | O |
| 1 | 28.38 | 14.27 | 57.35 |
| 2 | 28.44 | 14.35 | 57.21 |
| 3 | 28.50 | 14.45 | 57.05 |
| 4 | 28.42 | 14.28 | 57.30 |
| white spot | 39.30 | 0.31 | 60.40 |
| 1 s.d. | 0.05 | 0.08 | 0.13 |
| Average | 28.44 | 14.34 | 57.23 |
| Comp. | 1.99 | 1.00 | 3.99 |

Figure 6. Electron Probe Microanalysis Results for $La_2NiO_{4+\delta}$. Analysis points were selected randomly.

The cell parameters for a series of compositions $La_xPr_{2-x}NiO_{4+d}$ (x = 2, 1.9, 1.2, 1.0 and 0) are shown in Figure 7. Substitution of praseodymium for lanthanum leads to an overall decrease of the cell volume consistent with the respective ionic radii. $La_2NiO_{4+\delta}$ and $Pr_2NiO_{4+\delta}$ are isostructural, but the ionic radius of $La^{3+}$ (r = 1.16 Å) is a little larger than that of $Pr^{3+}$ (r = 1.126 Å). The change in the non-stoichiometry (δ) also needs to be taken into account.

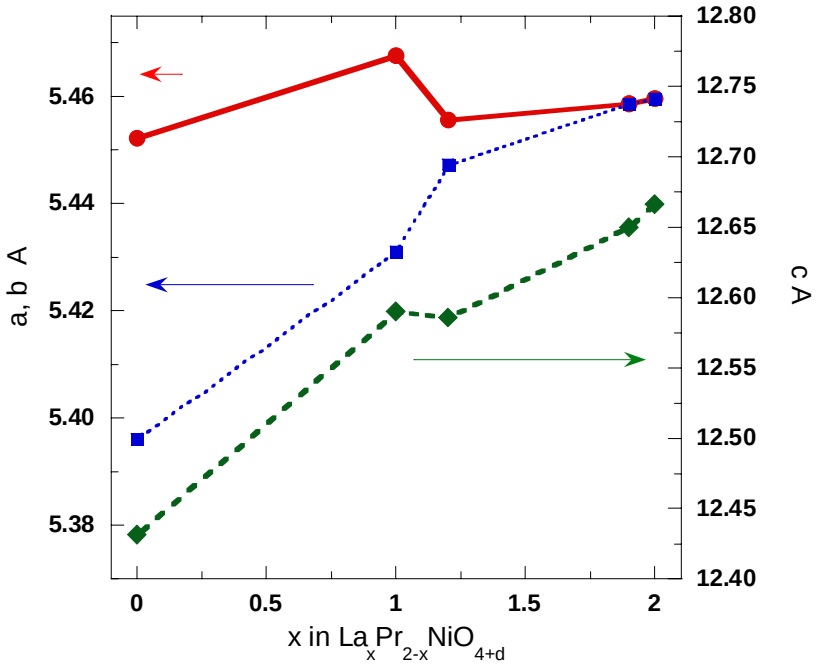


Figure 7. Cell parameters a, b and c (Å) versus x in $La_xPr_{2-x}NiO_{4+\delta}$

A TA Instruments 2950 thermobalance was used to determine the equilibrium non-stoichiometry and thermodynamic factor ($\Gamma$) of $La_xPr_{2-x}NiO_{4+\delta}$ as a function of temperature and oxygen partial pressure within the range of $0.01 \leq pO_2 \leq 0.07$ atm and 25 °C $\leq T \leq$ 950 °C. Measurements of the relative values of d in $La_xPr_{2-x}NiO_{4+\delta}$ obtained from thermogravimetric analysis were placed on an absolute basis by determining the starting composition using iodometric titration. The results are shown in Figure 8 for all compositions. In the temperature range of interest, 500-700 °C, all compositions have significant concentrations of interstitial oxygen ions. At the same temperature and $pO_2$ the interstitial oxygen ion concentration is greater in $Pr_2NiO_{4+\delta}$ than in $La_2NiO_{4+\delta}$.

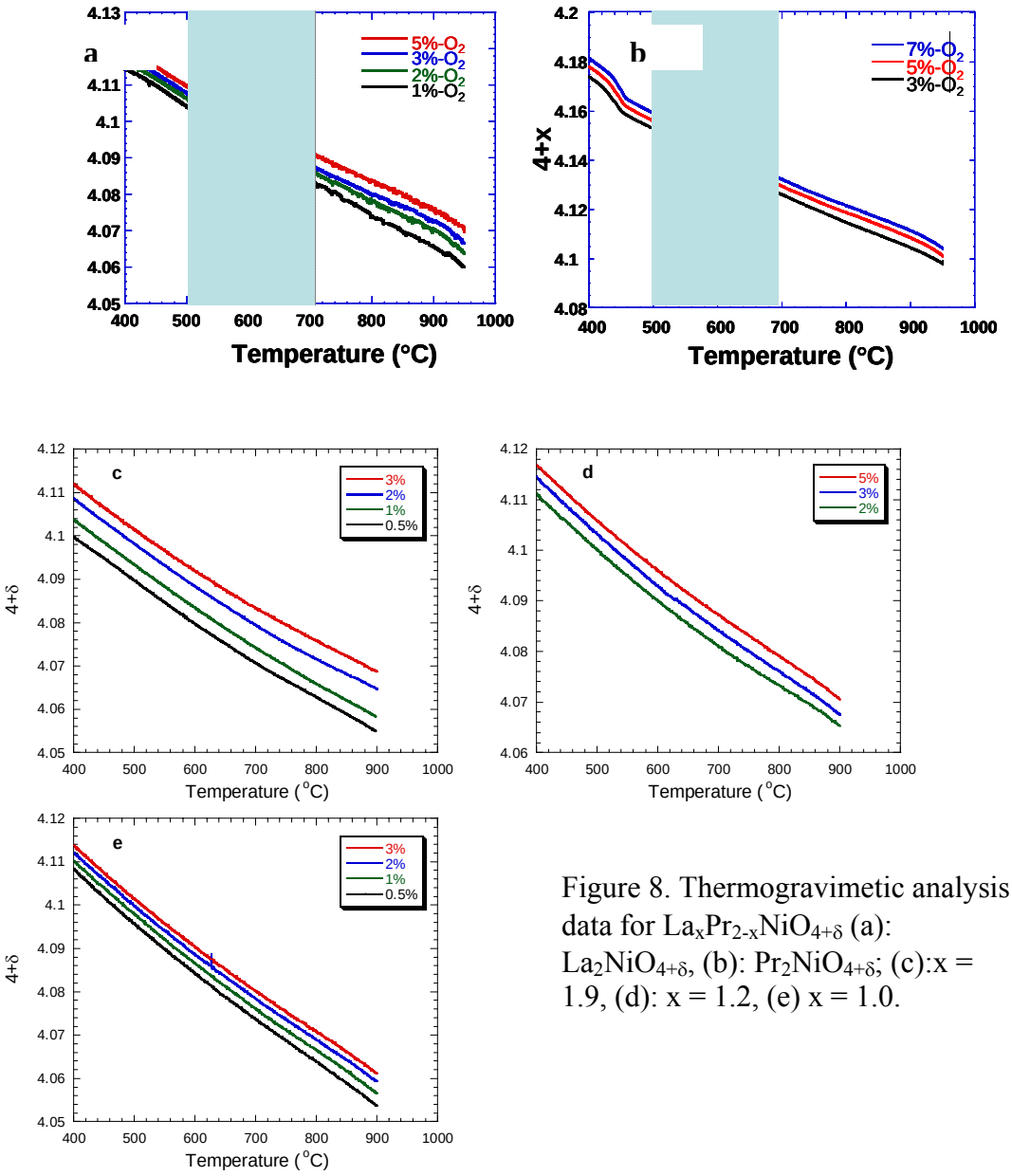


Figure 8. Thermogravimetic analysis data for $La_xPr_{2-x}NiO_{4+\delta}$ (a): $La_2NiO_{4+\delta}$, (b): $Pr_2NiO_{4+\delta}$; (c):x = 1.9, (d): x = 1.2, (e) x = 1.0.

### 4.2.4 DC Conductivity Measurements

Rectangular shaped bars for $La_2NiO_{4+d}$ (16.0 × 1.6 × 1.7 mm), $La_{1.9}Pr_{0.1}NiO_{4+\delta}$ (12.6 × 1.6 × 2.0 mm), $La_{1.2}Pr_{0.8}NiO_{4+\delta}$ (12.9 × 1.7 × 2.2 mm), $LaPrNiO_{4+\delta}$ (12 × 2.1 × 1.9 mm) and $Pr_2NiO_{4+d}$ (18.0 × 1.8 × 2.1 mm) were cut for DC conductivity. The densities of the bars measured by the Archimedes method were > 90 %.

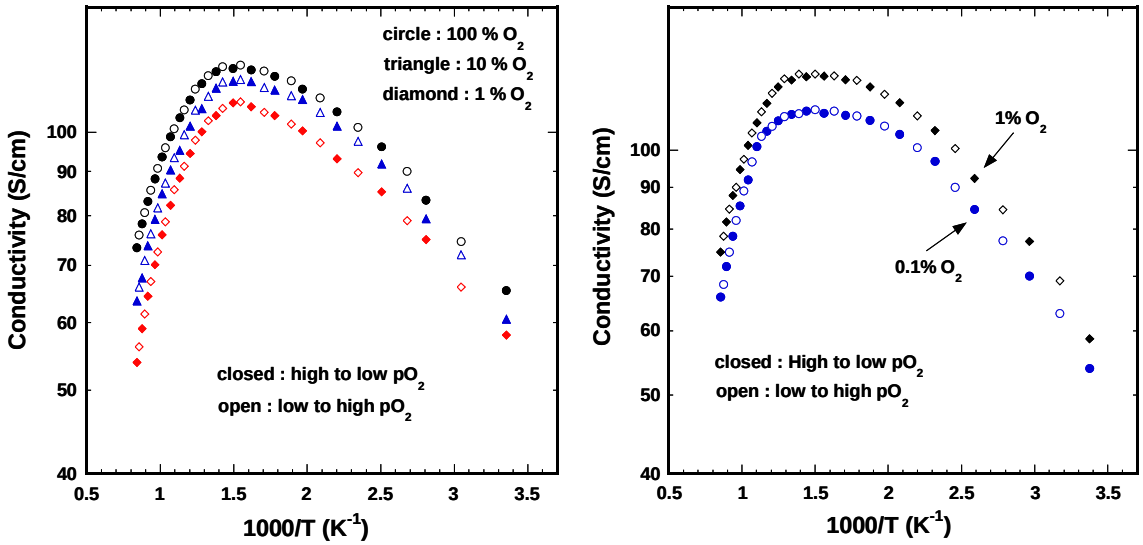


Figure 9. The total conductivity of $La_2NiO_{4+\delta}$ (left) and $Pr_2NiO_{4+\delta}$ (right).

The total conductivity results are shown in Figure 9. The data show typical behavior for p-type conductors that lose oxygen atoms on heating. At near ambient temperature, the data show Arrhenius behavior but above ~200 °C, the rate of increase of the conductivity begins to decrease. This temperature is about 100-150 °C lower than most perovskite oxides implying faster oxygen exchange kinetics. The maximum conductivity in both cases is about 200 $Scm^{-1}$, a reasonable value for use of the materials as SOFC cathodes.

In three other compositions (x = 1.9, 1.2 and 1), each composition has a high conductivity (~ 100 S/cm) in 0.1 and 0.01 $pO_2$ atm (see Figure 10.) and a different roll over temperature where oxygen loss offsets the effect of increasing temperature (315 K for $LaPrNiO_{4+\delta}$, 450 K for $La_{1.2}Pr_{0.8}NiO_{4+\delta}$, and 320 K for $La_{1.9}Pr_{0.1}NiO_{4+\delta}$, respectively). The results for all compositions measured in 1% oxygen are shown in Figure 11 (left). With increasing substitution of Pr into La, the conductivity increases after an initial large decrease from the value for pure $La_2NiO_{4+\delta}$. Some evidence for a correlation with changes in the cell constants can be seen in Figure 11 (right) which has an abrupt change of conductivity between x = 1 ~ 1.2. The origin of this discontinuity is not yet known but may reflect a miscibility gap.

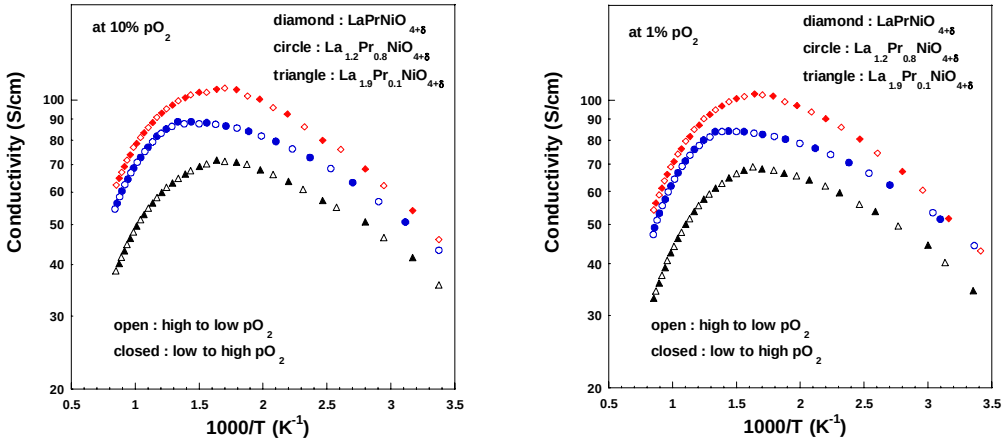


Figure 10. Conductivity data for $La_xPr_{2-x}NiO_{4+\delta}$ (x = 1.9, 1.2 and 1) at 10 % and 1 % $pO_2$

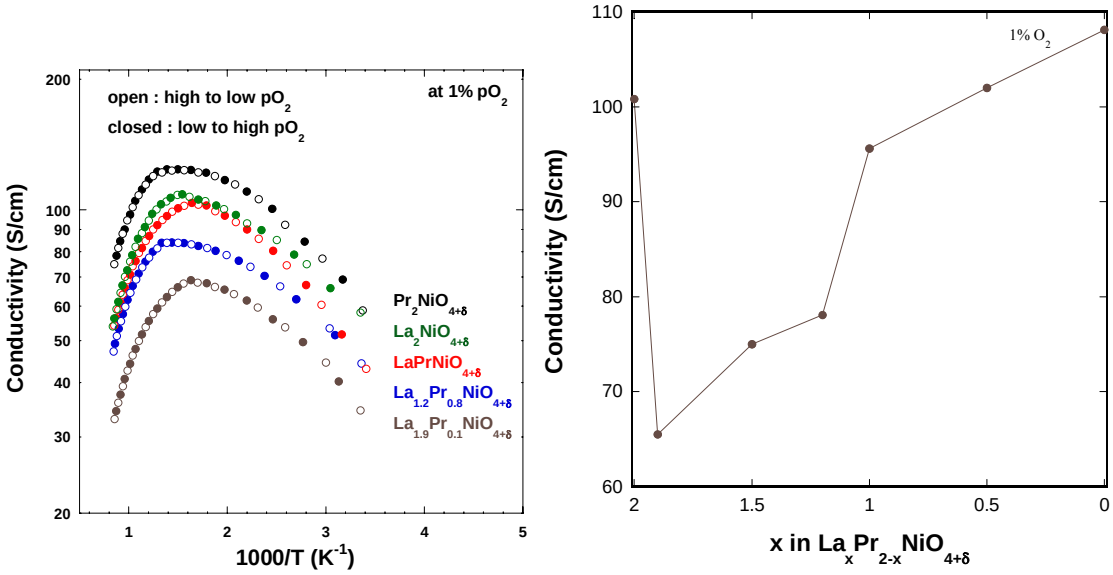


Figure 11. Comparison of the DC conductivities for $La_xPr_{2-x}NiO_{4+\delta}$ vs. temperature and vs composition at 1000/T = 2.0.

### 4.2.5 Electrical Conductivity Relaxation Measurements

Electrical conductivity relaxation measurements were made using an experimental apparatus and analysis procedure that we have previously reported.[10] A typical relaxation curve for $La_2NiO_{4+\delta}$ is shown in Figure 12 for a pressure switch between 0.01 and 0.02 atm at 800 °C. The open symbols are the data and the continuous line the experimental fit

with two parameters $D_{chem}$ and $k_{chem}$. The difference between the data and the calculated fit are shown also (error) and indicate excellent agreement of the data with the model.

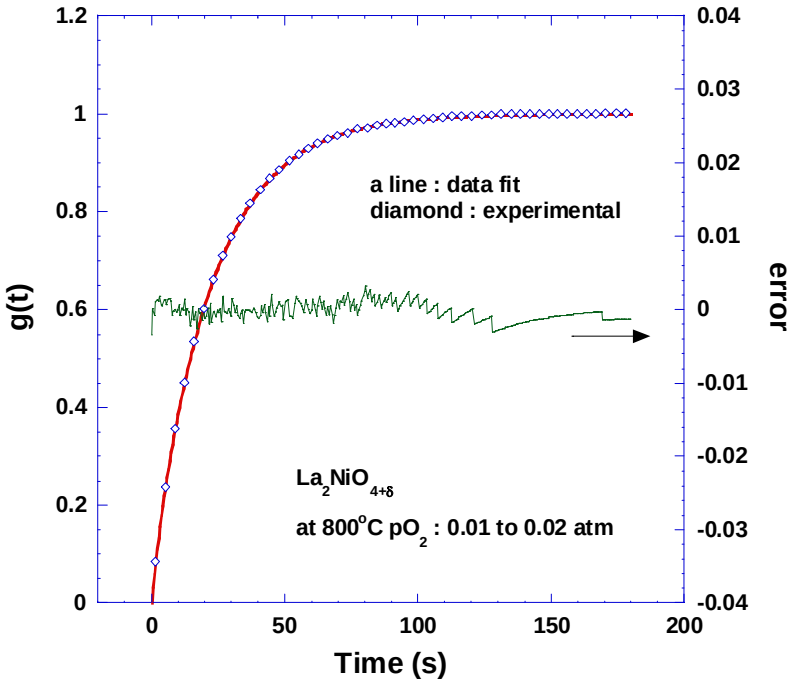


Figure 12. Typical conductivity relaxation data for $La_2NiO_{4+\delta}$

Results for the chemical diffusion coefficient $D_{chem}$ for several different pressure switches as a function of temperature are shown in Figure 13 (left) for both $La_2NiO_{4+\delta}$ and $Pr_2NiO_{4+\delta}$. The results show some dependence on the final pressure of the switch in both cases. This is primarily associated with small changes in the thermodynamic factors in this pressure range. The pressure dependence disappears when the oxygen ion diffusion coefficients are calculated according to $D_O = D_{chem} / \Gamma$ where $\Gamma$ is the thermodynamic factor as shown in Figure 13 (right). It is apparent in Figure 6 that $D_O$ for the praseodymium compound is higher that for $La_2NiO_{4+\delta}$. The values of $D_O$ for both compounds have similar activation energies. In Figure 14, the present results are compared with previous results obtained by isotope exchange and depth profiling (IEDP) which show the same trend in that $D_O$ ($Pr_2NiO_{4+\delta}$) > $D_O$ ($La_2NiO_{4+\delta}$). In contrast, the values of $k_{ex}$ are quite different in both magnitude and activation energy. The reason for this is not yet known but is important because the $k_{ex}$ values that we measure would be expected to give much lower electrode resistances. We later carried out additional AC impedance experiments to confirm our measured values. It is important to keep in mind that the surface exchange coefficient is likely to be sensitive to sample preparation conditions, surface compositions and the presence of impurity phases.

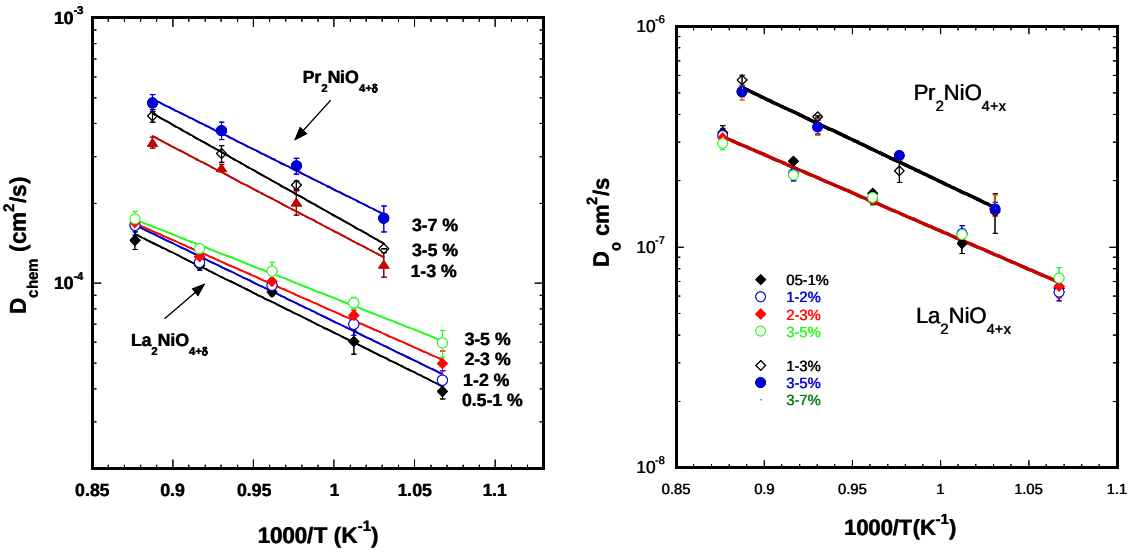


Figure 13. Values of $D_{chem}$ (left) and $D_O$ (right) determined by Electrical Conductivity Relaxation

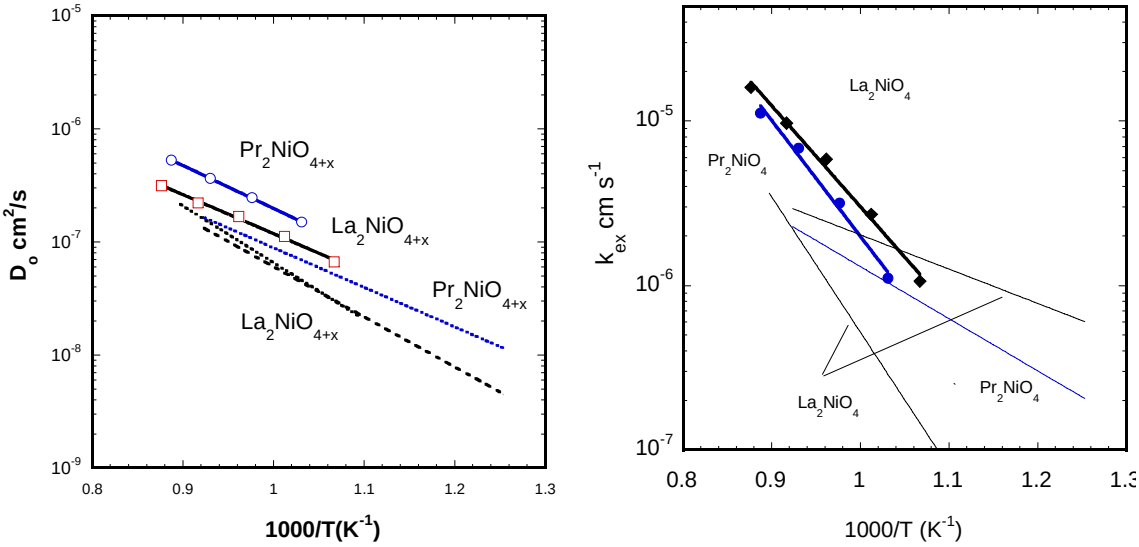


Figure 14. Comparison of the present results with the IEDP data of reference 3 and 11

Electrical conductivity relaxation measurements were also made for the new K1 compositions $La_xPr_{2-x}NiO_{4+\delta}$ (x = 1.9, 1.2 and 1.0) and the results for $D_{chem}$ and $k_{chem}$ are shown in Figure 15. For $D_{chem}$, the activation energies for each composition are similar. Much wider variations are observed in both the activation energy and magnitude of $k_{chem}$. $La_{1.9}Pr_{0.1}NiO_{4+\delta}$ has the highest value of $k_{chem}$ but $LaPrNiO_{4+\delta}$ has both a high value of $k_{chem}$ and a low activation energy.

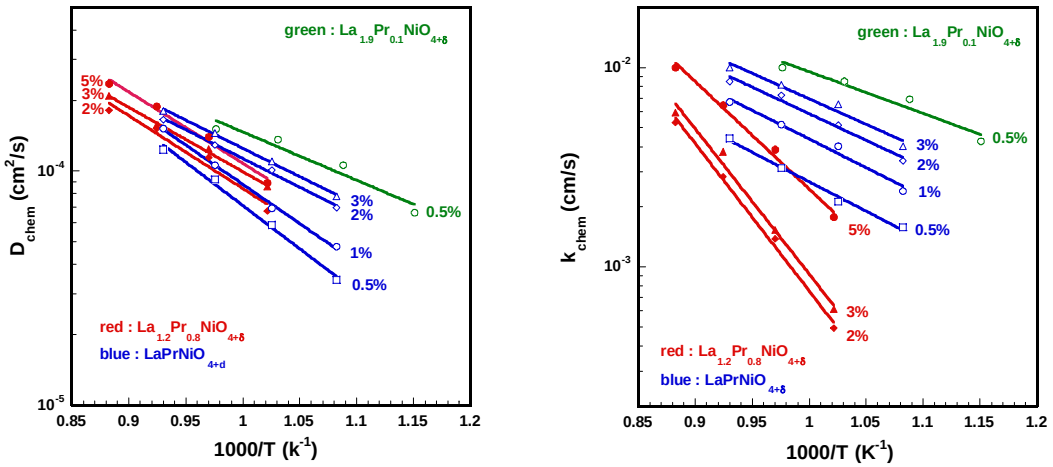


Figure 15. Values of $D_{chem}$(left) and $k_{chem}$(right) of $La_xPr_{2-x}NiO_{4+\delta}$ (x = 1.9, 1.2, 1)

The results from the TGA measurements were used to convert the values of $D_{chem}$ and $k_{chem}$ reported previously using the relations $D_O = D_{chem} / \Gamma$ and $k_{ex} = k_{chem} / \Gamma$ where $\Gamma$ is the thermodynamic factor. The results are shown in Figure 16.

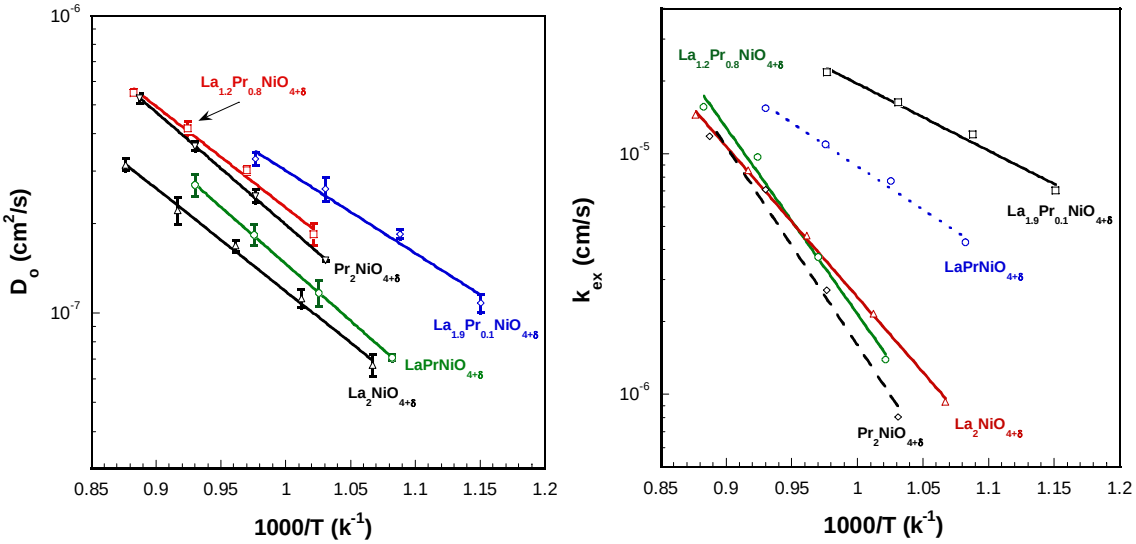


Figure 16 Values of $D_o$ (left) and $k_{ex}$ (right) at 3 % $pO_2$ except 0.5 % for $La_{1.9}Pr_{0.1}NiO_{4+\delta}$ determined by electrical conductivity relaxation

The diffusion coefficients vary by about a factor of 2 with $La_{1.9}Pr_{0.1}NiO_{4+\delta}$ being the highest and $La_2NiO_{4+\delta}$ the lowest. The activation energies are similar within the experimental errors. In contrast, much more variation is found in the surface exchange

velocities. Two compositions $La_{1.9}Pr_{0.1}NiO_{4+\delta}$ and $La_{1.0}Pr_{1.0}NiO_{4+\delta}$ were found to have much higher $k_{ex}$ values at low temperature and lower activation energies.

### 4.2.6 Reactions of $La_2NiO_4$ and $Pr_2NiO_4$ with GDC and YSZ

The phase compatibility of $La_2NiO_4$ and $Pr_2NiO_4$ with YSZ and GDC electrolytes was investigated by solid state reaction and powder X-ray diffraction. The powder X-ray diffraction pattern of a mixture of $La_2NiO_4$ (LNO) and YSZ after heat treatment at 1075 °C is shown in Figure 17. X-ray data for a LNO/YSZ mixture after heat treatment at 1075 °C. The diffraction data shows clear evidence for extensive conversion of the starting phases and the formation of $La_2Zr_2O_7$. The reactivity of $La_2NiO_4$ and CGO (10% gadolinium) and $Pr_2NiO_4$(PNO)and CGO are shown by the X-ray diffraction patterns in Figure 18. No reaction between $La_2NiO_4$ and CGO occurs at 850 °C, but a second phase appeared at 900 °C. For $Pr_2NiO_4$, the second phase appears at 800 °C.

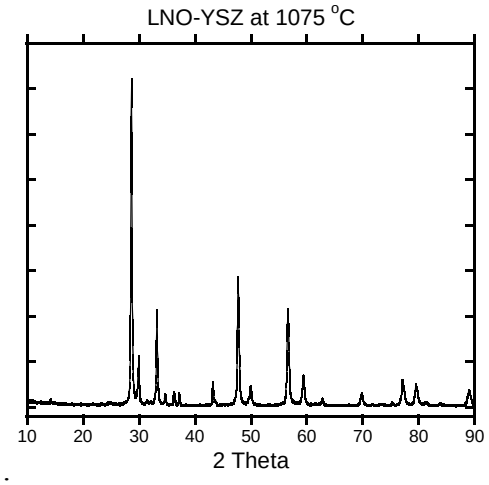


Figure 17. X-ray data for a LNO/YSZ mixture after heat treatment at 1075 °C

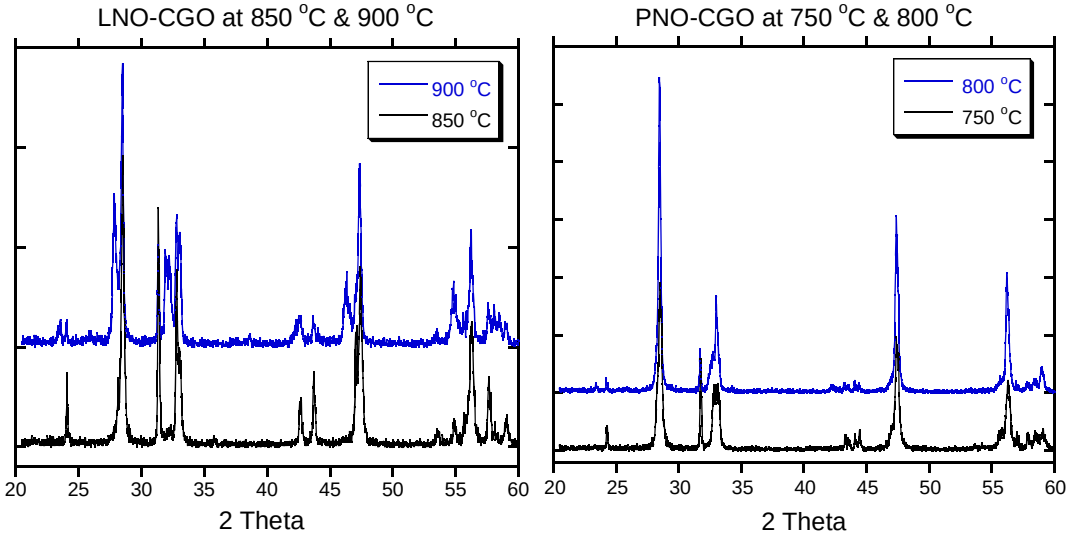


Figure 18. X-ray diffraction patterns of mixtures of LNO-CGO and PNO-CGO after heat treatments.

### 4.2.7 Symmetric cell measurements

Gadolinia doped cerium oxide (CGO) containing 10 % gadolinia powder was purchased from Rhodia. The powder was cold isostatically pressed into pellets at 40,000 psi and sintered in air at 1350 °C for 10 h. The pellet density was greater than 95 % of the theoretical value. The electrode powders were made into ink, and used to fabricate symmetrical LNO/CGO/LNO cells with 1 $cm^2$ active area. The electrodes were sintered at 1000 °C in air for 2h. Gold gauze was used as the current collector on both electrodes. The symmetrical LNO/CGO/LNO cell and the Au gauzes were pressed together physically with spring loading. Electrochemical impedance spectra were obtained using a Solatron 1260 frequency response analyzer. The applied frequency ranged from 2MHz to 0.1 Hz.

Typical impedance spectra obtained with a symmetrical cell under various oxygen partial pressures at 527 °C are shown in Figure 19. The intercepts with the real axis will be referred to $R_{elecrolyte}$, which is independent of $pO_2$ in the high frequency region, and $R_{elecrode}$ in the low frequency region. The low-frequency contribution whose amplitude depends on the oxygen partial pressure was attributed to the cathode reactions. The area specific resistance (ASR) is calculated as half the difference between the low and high frequency intercepts with the real axis (Figure 20). The ASR is then given by ASR = ($R_2$ - $R_1$)*S/2, where $R_2$ and $R_1$ are low frequency intercept and high frequency intercept, respectively, and S is the geometrical surface area of the symmetrical cell.

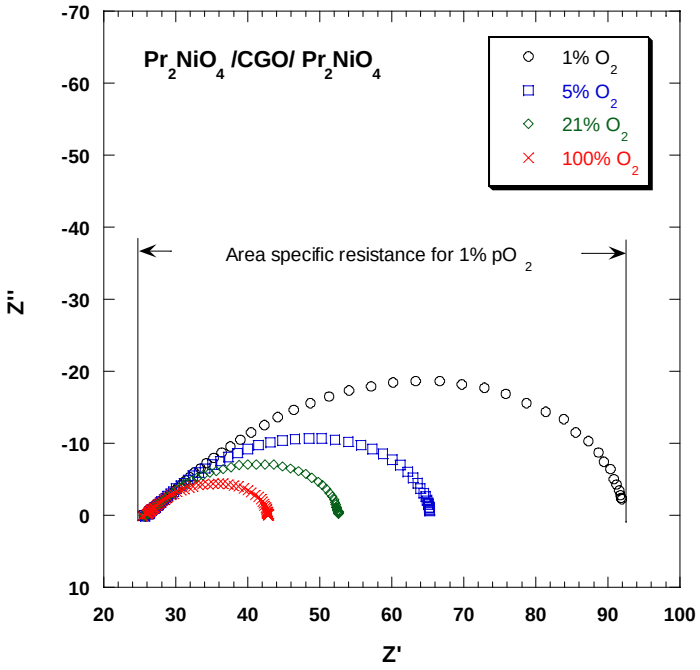


Figure 19. Representative impedance spectra of the $Pr_2NiO_{4+\delta}$ electrochemical cell: $Pr_2NiO_{4+\delta}$ /CGO/ $Pr_2NiO_{4+\delta}$ (T= 527 °C).

The performance target for new oxide cathode materials is 1.0 W/$cm^2$ at 0.7 V in with GDC electrolytes at 600 ºC. This translates to a total cell resistance of 0.5 Ω/$cm^2$. The

measured area specific resistance for the K1 cathodes $La_2NiO_{4+\delta}$ and $Pr_2NiO_{4+\delta}$ are shown in Figure 12.

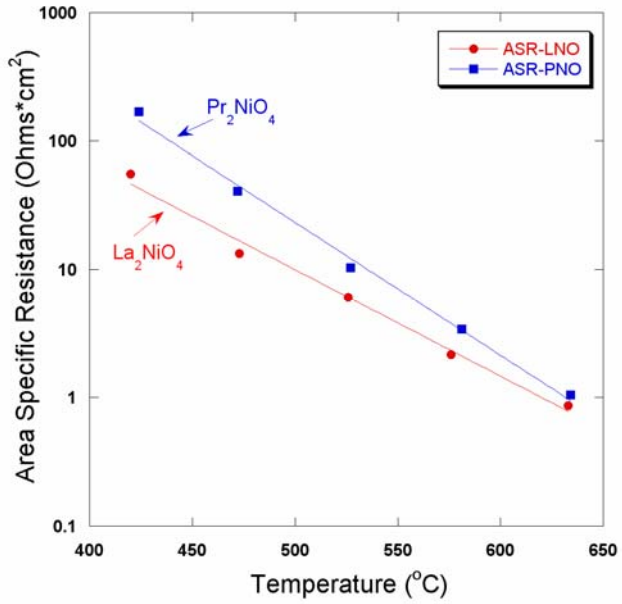


Figure 20. Area Specific Resistance vs. Temperature for $La_2NiO_{4+\delta}$ and $Pr_2NiO_{4+\delta}$

The results for these non optimized electrodes are encouraging and suggest that with further optimization of the electrode structure may enable the target to be reached. This is also suggested by an estimate of the ASR based on the previously measured values of D and k.

The change in area specific resistance as a function of oxygen partial pressure can be represented by $1/ASR = 1/ASR^0 (pO_2)^m$. The exponent m is 0.27 ~ 0.31 at 526 °C ≤ T ≤ 634 °C for LNO and PNO system as shown in Figure 21.

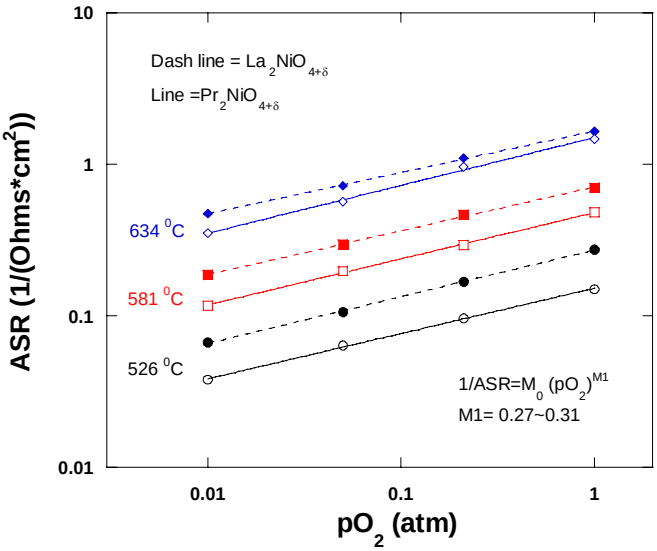


Figure 21. The variation of the ASR with oxygen partial pressure at different temperatures.

### 4.2.8 Half cell measurements of PNO and LNO electrodes

Peter C. Rieke and Zimin Nie (Pacific Northwest National Laboratory)

Powders provided by UH were ball milled for 48 h. Sintering studies were conducted for LNO, PNO on YSZ. From this study appropriate sintering temperatures were used to prepare films on SDC. The temperatures used were LNO -- 2 h at 1200 °C and PNO -- 2 h at 1150 °C

SDC power was compressed in a die, sintered at 1200 °C for 2 h. The diameter was ground to 13 mm diameter and both faces were ground flat and parallel to a thickness of about 3 mm. A blind hole for insertion of the reference electrode was drilled from one side to within less than 1 mm of the other surface. The working electrodes were prepared by screen printing the inks described above on the undrilled surface and fired at the given temperature. Pt ink for the counter electrode was then screen printed on the drilled side and fired for 1 hr at 1000 °C. The samples were then inserted into the test rig and brought to 850 °C in 3 h. Samples were tested at 850, 750, 650 and 600 °C. The 600 °C for LNO were suspect and the pellet probably cracked (as determined upon disassembly) prior to obtaining the data.

The electrochemical response was tested by cyclic voltammetry at 1 mV/sec scan rate and with potential limits that kept the current under about 1.5 Amps. Current interrupt with a 27 μs time delay was used to remove the series resistance usually associated with the electrolyte resistance. AC impedance spectra were also obtained using a 10 mV input stimulus at zero potential bias. Tests were conducted with air and oxygen flowing at 1 ml/min. The data were fit to a circuit consisting of a simple resistor and two constant phase elements (CPE) all in series. At the higher temperatures the data showed two distinct arcs. The fit was better for two CPE than with two simple RC elements or with one CPE. For consistency the fit to two CPE was used for all data although some data did not show distinct arcs. The quality of the CV data is affected by the current interrupt technique. The series resistance is approximately 1 ohm at 850 °C while the Faradaic resistance is about .2 to .3 ohm. Small errors in compensating for the large Rs values result in much larger errors in the Faradaic resistances. The results are summarized in Figure 22 and compared with the results obtained with symmetrical cells. The results at the two different oxygen partial pressures are consistent. For LNO, the data from the impedance and CV measurements on half cells are reasonably consistent and are larger by a factor of five compared with the values from the symmetric measurements. The reason for this is most likely due to differences in electrode microstructures and requires additional study. For PNO, the results at 850 and 750 °C for the half cells lie on an extrapolation of the symmetric cell data. However, the data at lower temperatures indicate much higher electrode resistances for reasons that are not understood. The difference in the electrode resistance between LNO and PNO is apparent in the half cell cyclic voltammetry measurements shown in Figure 23.

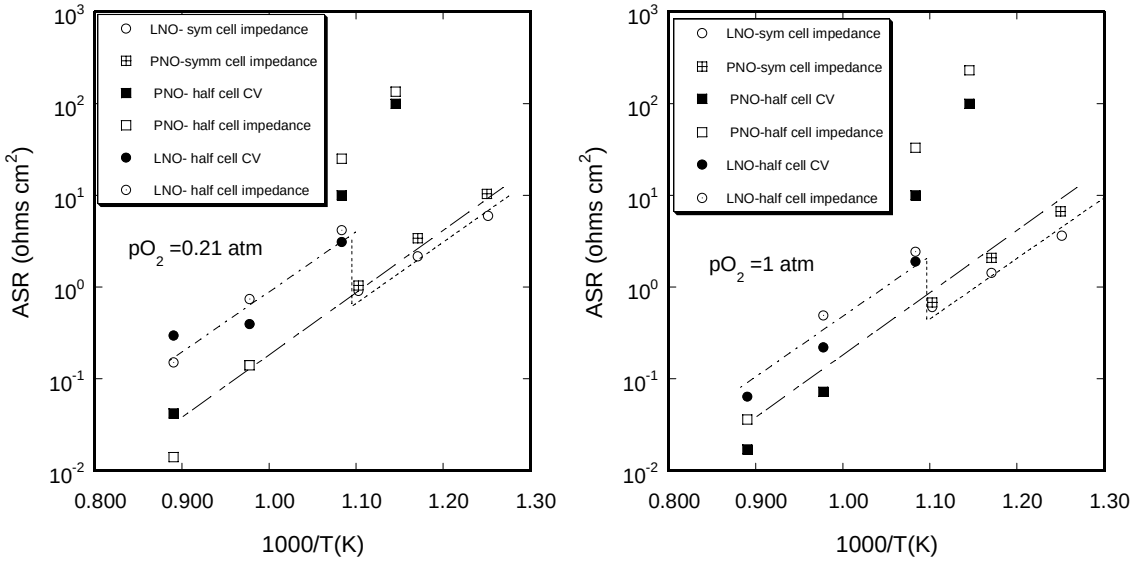


Figure 22. A comparison of measurements of the electrode resistance of LNO and PNO at $pO_2$ = 0.21 atm (left) and 1 atm (right).

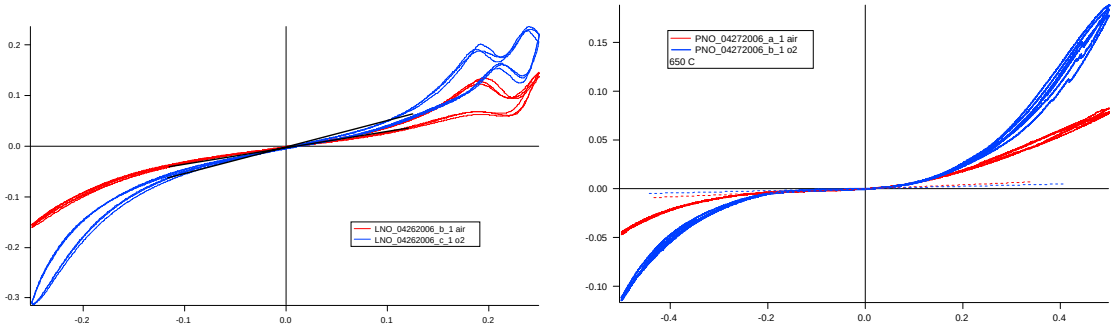


R_LNO_650_$O_2$ = 1.90 ohms
R_LNO_650_air = 3.11 ohms

R_PNO_650_air = 48 ohms
R_PNO_650_$O_2$ = 88 ohms

Figure 23 Cyclic voltammetry measurements for LNO and PNO at 650 °C showing the large difference in performance.

### 4.3 P2 compositions $LnBaCo_2O_{5+\delta}$

#### 4.3.1 Synthesis of P2 compositions $LnBaCo_2O_{5+\delta}$ (Ln = Pr and Nd)

In recent years, many oxide materials containing Mn, Fe, Co and Ni have been studied for use as cathode materials at intermediate operating temperatures. For the most part, these compositions can be represented by $(La,Sr)(B,B')O_{3-x}$ where B,B' = Mn, Fe, Co and Ni. A characteristic feature of these compounds is that the A site and B site cations are disordered. Disorder can be prevented by appropriate choice of the cation combinations. To induce A site order, it requires increasing the size difference between the two cations for example in Pr,Ba as distinct from La,Sr. A typical consequence of the A site order is that the oxygen vacancies also occupy specific sites as shown in Figure 24. In the specific example is the oxygen-deficient perovskite, $LnBaCo_2O_{5+\delta}$ (Ln = Pr and Nd). The oxygen content can be as high as $\delta = 0.7$ for samples synthesized in air.

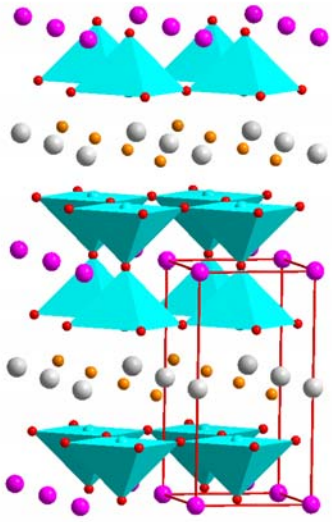

Figure 24. The structure of $LnBaCo_2O_{5+\delta}$; the purple and silver spheres represent the barium and lanthanide cations, the square pyramidal coordination of cobalt ions is shown in blue, and the partially occupied oxygen ion sites as orange spheres.

We have chosen this structure type as our second class of perovskite compositions (P2). In the initial studies $LnBaCo_2O_{5+\delta}$ (Ln = Pr and Nd) compounds were synthesized via a citrate precursor method. Stoichiometric amounts of $Pr_6O_{11}$ (Alfa 99.99 %) and $Nd(NO_3)_2$, and cobalt nitrates (Aldrich, 99.99 %), were dissolved in dilute nitric acid. Ethylene glycol (EM science >98 %) and citric acid (Aldrich, 99.5 %) were added to the solution. This mixture was covered and stirred at 150 °C until the solution began to foam and formed a dry resin. Further heating at 300 °C and then 600 °C for 24 h periods decomposed the dry foam containing residual organic components. The final mixture was pressed into a 1-inch diameter die followed by cold isostatic pressing (CIP). The pellet

was sintered in air at 1100 °C for 12 h and then cooled down slowly in nitrogen. Finally a rectangular shape bar (16.0 × 2.4 × 1.7 mm) was cut for DC conductivity and ECR measurements.

### 4.3.2 Characterization of $LnBaCo_2O_{5+\delta}$ (Ln = Pr and Nd) (XRD & TGA)

X-ray powder diffraction measurements (Scintag XDS 2000) with Cu Kα radiation were performed to confirm the structure and the powder patterns were indexed by Rietveld refinement using GSAS program (Figure 25 for Pr). A scan rate of 0.125°/min was used with the range $5° \leq 2\theta \leq 90°$. The refined lattice parameters were a = 3.9084(1) Å, b = 3.9053(1) Å, c = 7.6343(2) Å for $PrBaCo_2O_{5.7}$ and a = 3.8057(1), Å b = 3.9045(1) Å, c = 7.7893(3) Å for $NdBaCo_2O_{5.7}$ .

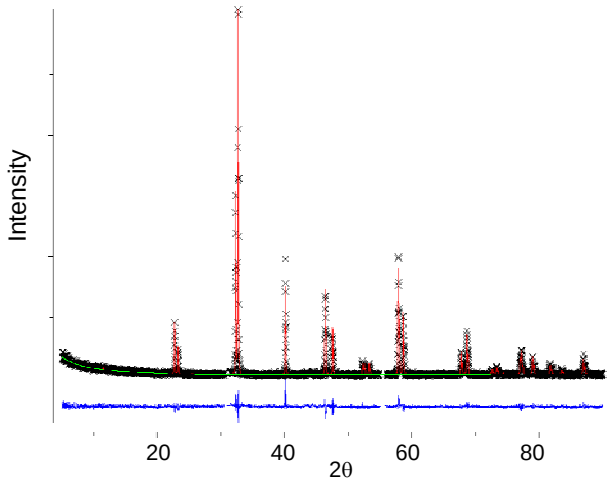


Figure 25. Rietveld refinement of $PrBaCo_2O_{5.7}$

A TA Instruments 2950 thermobalance was used to determine the equilibrium non-stoichiometry and thermodynamic factor (Γ) as a function of temperature and oxygen partial pressure within the range of $0.01 \leq pO_2 \leq 0.21$ atm and $25 \leq T \leq 800$ °C.

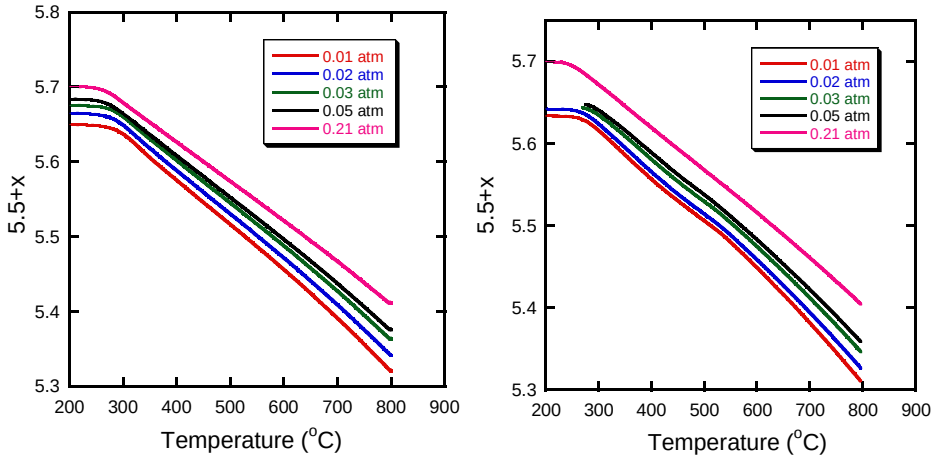


Figure 26. Thermogravimetric analysis of $LnBaCo_2O_{5+\delta}$ (Ln = Pr, Nd).

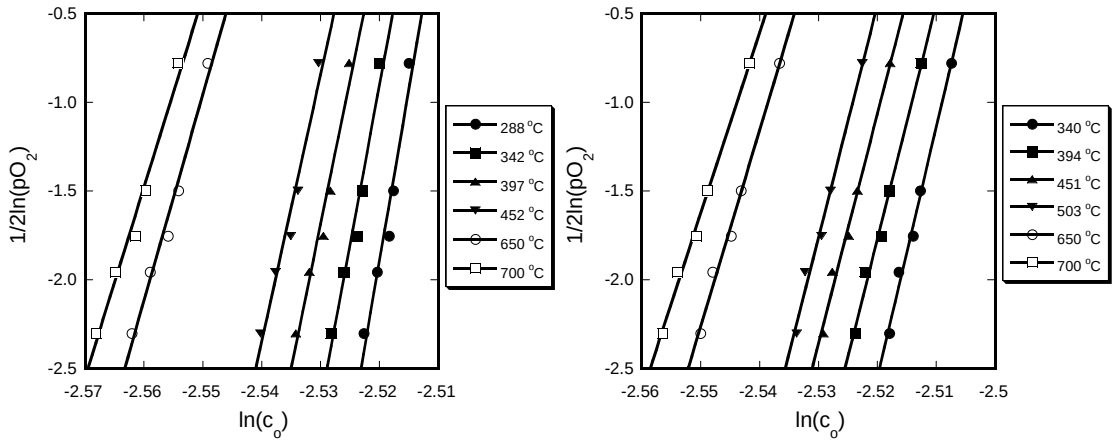


Figure 27. The thermodynamic factors for $PrBaCo_2O_{5+\delta}$ (left)and $NdBaCo_2O_{5+\delta}$ (right).

The thermodynamic factors for $PrBaCo_2O_{5+\delta}$ and $NdBaCo_2O_{5+\delta}$, are shown in Figure 27. The thermodynamic factors were derived from the thermogravimetric data according to

$$\Gamma_O = \frac{\partial \ln a_O}{\partial \ln c_O} = \frac{1}{2}\frac{\partial \ln pO_2}{\partial \ln c_{O^{2-}}} \qquad (1)$$

Table 3 summarizes the thermodynamic factors for $LnBaCo_2O_{5.5+x}$ (Ln = Pr, Nd). As the temperature increases, the values of the thermodynamic factor decrease. The values of the TDFs of $NdBaCo_2O_{5.5+x}$ are systematically smaller than those of $PrBaCo_2O_{5.5+x}$ over this temperature range.

**Table 3. Summary of the thermodynamic factors for $LnBaCo_2O_{5+\delta}$ (Ln = Pr, Nd)**

| $PrBaCo_2O_{5+\delta}$ | | $NdBaCo_2O_{5+\delta}$ | |
|---|---|---|---|
| Temperature (ºC) | Γ | Temperature (ºC) | Γ |
| 288 | 193(26) | 340 | 141(8) |
| 342 | 179(22) | 394 | 132(8) |
| 397 | 162(19) | 451 | 129(8) |
| 452 | 150(17) | 503 | 131(9) |
| 650 | 116(10) | 650 | 110(6) |
| 700 | 107(9) | 700 | 102(5) |

### 4.3.3 DC Conductivity of $LnBaCo_2O_{5+\delta}$ (Ln = Pr and Nd)

The total conductivities were measured on rectangular bars of $PrBaCo_2O_{5+\delta}$ (PBCO, 1.3×0.19×0.15 cm) and $NdBaCo_2O_{5+\delta}$ (NBCO, 1.4×0.2×0.21 cm). Results are shown in Figure 28. As the temperature is increased, the conductivities begin to decrease at ~150 ºC due to the loss of oxygen atoms from the lattices and reduction of Co(IV) to Co(III). The data indicate that the onset temperature for oxygen loss is slightly lower for the Nd compound. Conductivity reaches a maximum value of 2000 and 1000 S/cm for $PrBaCo_2O_{5+\delta}$ and $NdBaCo_2O_{5+\delta}$, respectively

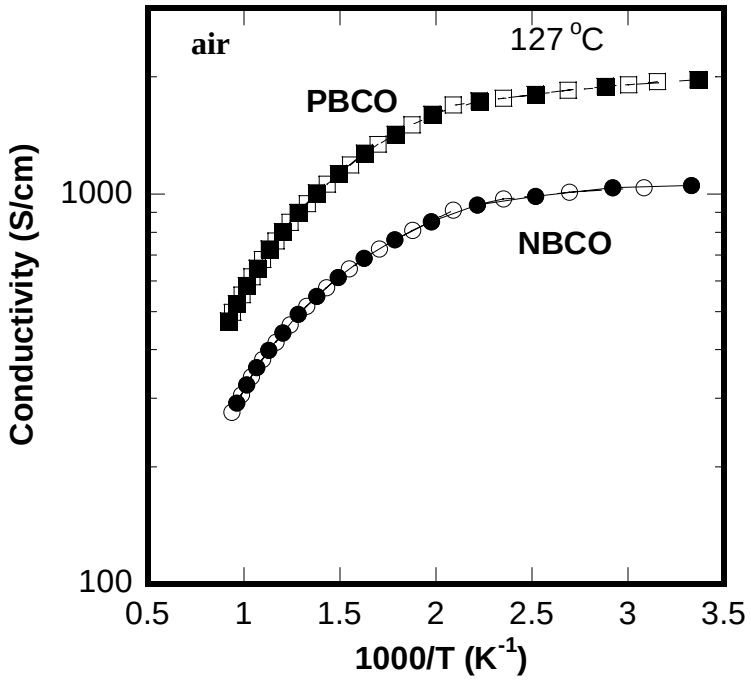


Figure 28. Total conductivity of $LnBaCo_2O_{5+\delta}$, (Ln=Pr, Nd).The open and closed symbols correspond to measurements on increasing and decreasing temperature.

### 4.3.4 ECR Studies of $LnBaCo_2O_{5+\delta}$ (Ln = Pr and Nd)

The diffusion coefficients and surface exchange coefficients were measured for $LnBaCo_2O_{5+\delta}$ (Ln = Pr, Nd) by electrical conductivity relaxation (ECR). ECR was performed on the same sample as used for the DC conductivity measurements. Results are shown in Figure 29. Values of $k_{chem}$ of both samples are similar while their $D_{chem}$ has different values and activation energy. The self diffusion coefficient, $D_o$, and self surface exchange coefficient, $k_o$ are plotted in Figure 30. Since these two compositions have similar thermodynamic values, the trend of $D_o$ and $k_o$ are similar to $D_{chem}$ and $k_{chem.}$

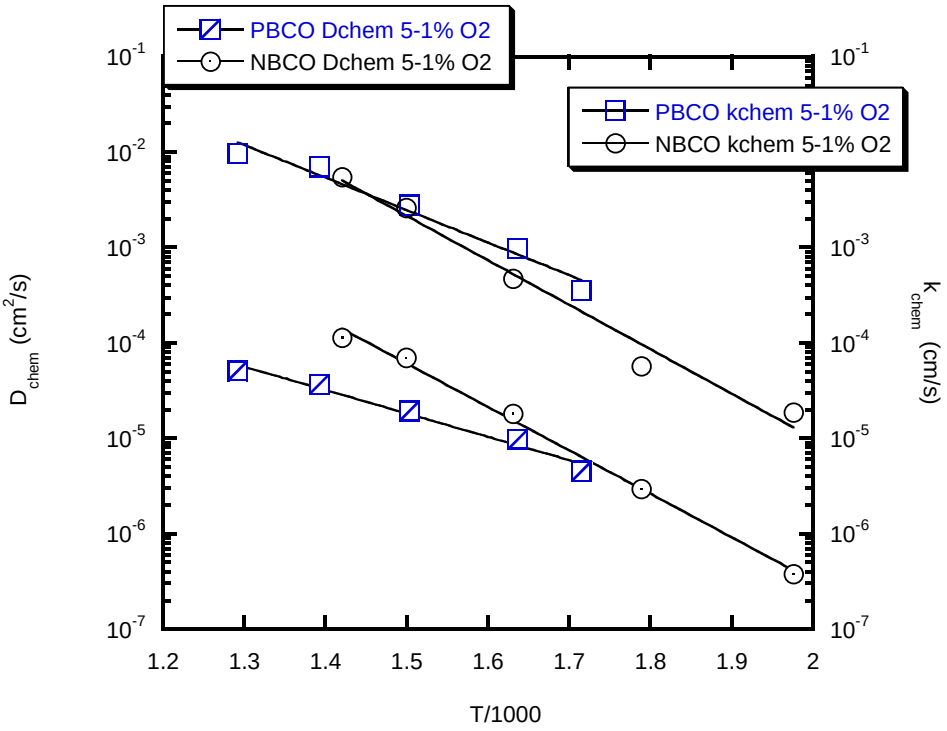


Figure 29. $D_{chem}$ and $k_{chem}$ obtained for $LnBaCo_2O_{5+\delta}$ (Ln = Pr, Nd).

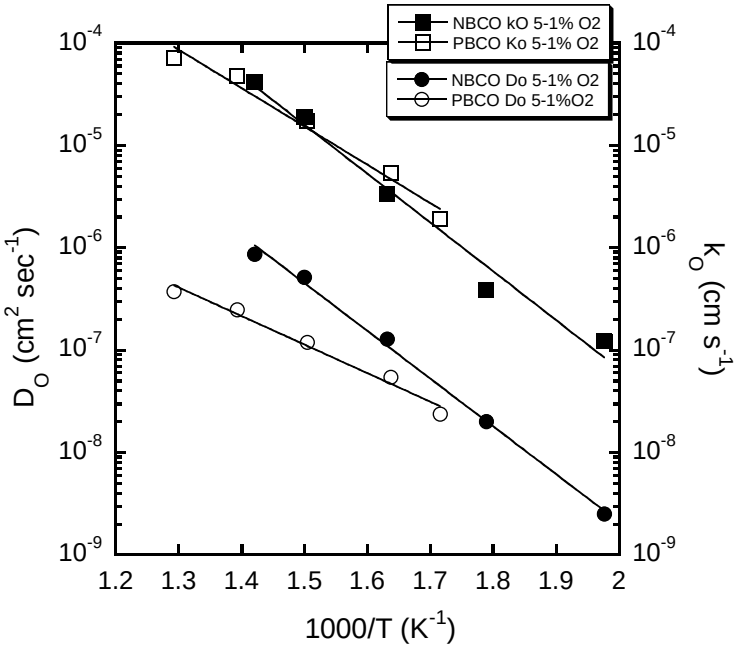


Figure 30. The temperature dependence of the self-diffusion ($D_O^{2-}$) and surface exchange coefficients ($k_{ex}$) for $LnBaCo_2O_{5.5+x}$ (Ln = Pr, Nd).

### 4.3.5 Isotope Exchange and Depth Profiling of $PrBaCo_2O_{5+\delta}$ (PBCO) ceramics.

The transport rates of oxygen were directly measured by $^{18}O$ IEDP. Rectangular samples were placed on a supporting quartz rod and inserted into a quartz reactor tube held in a tube furnace and purged by flowing oxygen (0.2 atm). The temperature was slowly (<5 ºC/min) raised to the experimental temperature and held there for at least one hour, after which the gas atmosphere was rapidly switched to $^{18}O_2$ (0.2 atm, 99% isotopic abundance) and then rapidly quenched by withdrawing the support rod and sample from the reactor. Imaging time-of-flight SIMS (ToFSIMS) analyses of both the exposed surfaces and also polished cross-sections of the infused materials were used to determine the resulting $^{18}O$ profile. Analysis chamber pressures less than 1 x $10^{-9}$ mbar were enforced during the SIMS analysis to avoid oxygen exchange with background gases. Values for the surface oxygen exchange coefficient, $k_O$, and the bulk oxygen self-diffusion coefficient, $D_O$, were obtained by fitting simulated profiles to the experimental data. The relationship between the transport parameters obtained by the IEDP and ECR is given by $(k \text{ or } D)_{chem}$ (ECR) / $\Gamma_O = (k \text{ or } D)_O$ where $\Gamma_O$ is the thermodynamic factor defined above.

Figure  shows one such section of one sample in both secondary electron (panel a) and $^{18}O$ fraction ($f^{18}O = {}^{18}O/({}^{18}O + {}^{16}O)$) SIMS signals (panel b). The resulting profile from this region and its fit are shown in panel c of Figure . The full cross-sectional ToF-SIMS images of $PrBaCo_2O_{5+\delta}$ were consistent with homogeneous transport properties in the ceramic material.

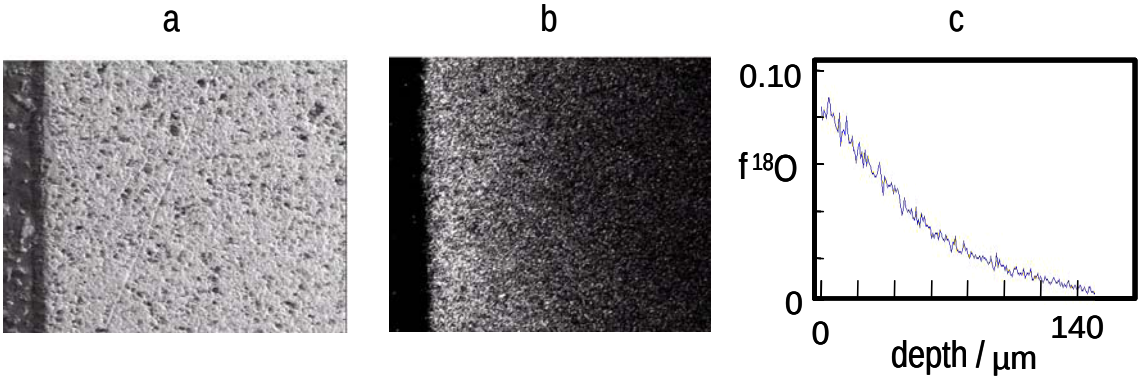


Figure 31. IEDP results for $PrBaCo_2O_{5+x}$ infused at 4000C for 5 min in 0.2 atm $^{18}O_2$ (99%). a: secondary electron image with $PrBaCo_2O_{5.5+\delta}$ region on the right and epoxy matrix on left. b SIMS image of the fraction of $^{18}O$, $f^{18}O = ({}^{18}O/({}^{18}O+{}^{16}O))$ of the same region as in panel a. c: the profile of $f^{18}O$ derived from the image in panel b.

A reproducible profile was seen around the perimeter(s) of the polished specimen(s), except for the region(s) where the sample was supported during infusion. A few cracks were evident in this material (not shown), but these were apparently created during quenching of the sample since no $^{18}O$ incorporation was seen at the crack surfaces. The $k_O$ and $D_O$ values derived from IEDP are somewhat higher than the ECR values – a factor of 2 for $D_O$.

The values of oxygen transport parameters $D_O$ and $k_O$ derived from the ECR data and the values of $\Gamma_O$ are shown in Figure 32 in comparison of the values of $D_O$ and $k_O$ measured by ECR for ceramic samples.

The reults are compared with data for othe perovskite materials. As noted above the isotope measurement for the diffusion coefficient is in good agreement with the ECR results. A significant discrepancy still remains between the corresponding values for $k_O$. Most significantly the values for both $D_O$ and $k_O$ are substantially higher that those reported for $La_{0.5}Sr_{0.5}CoO_3$, $La_{0.5}Sr_{0.5}FeO_3$ and $La_2NiO_4$.

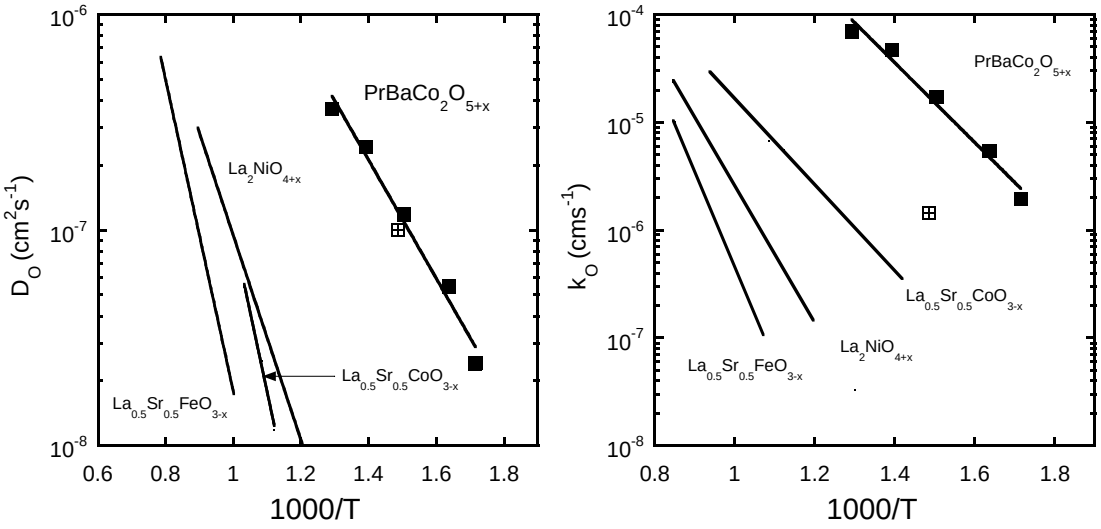


Figure 32. Comparison of the values of $D_O$ and $k_O$ with data for ceramic samples.

### 4.3.6 Reactions of $PrBaCo_2O_5$ with GDC and YSZ

A mixture of $PrBaCo_2O_5$ (PBCO) and CGO with weight % ratio of 75 to 25 was heat treated a various temperatures up to 1050 °C. No reaction between PBCO and CGO was observed even at 1050 °C (Figure 33).

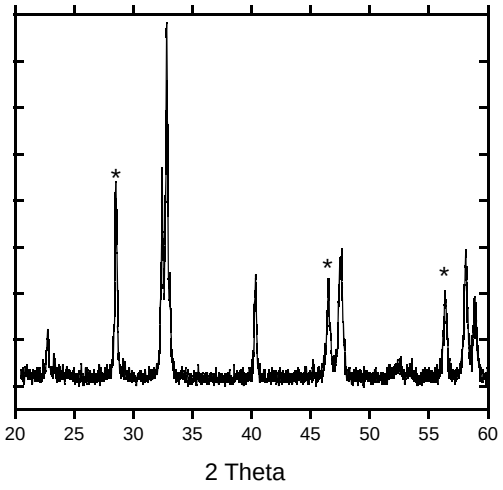


Figure 33. An X-ray diffraction pattern of 75-25 PBCO/CGO composite sintered at 1050 °C, * indicates CGO.

### 4.3.7 Impedance Measurements on Symmetric Cells

Gadolinia doped cerium oxide (CGO) powder containing 10 % gadolinia was purchased from Rhodia. The CGO-powder was cold isostatically pressed into pellets at 40,000 psi and sintered in air at 1350 °C for 10 h. The pellet density was greater than 96 % of the theoretical value. Films with the compositions 50 to 50 and 75 to 25 (PBCO to CGO) were made by tape-casting (Transionics Company) and used to fabricate symmetrical PBCO+CGO /CGO/PBCO+CGO cells with 1 $cm^2$ active area. The electrodes were sintered at 1100 °C in air for 2 h. Instead of using Pt, which is known to catalyze the oxygen reduction reaction, gold gauze was used as the current collector on both electrodes. The symmetrical PBCO+CGO/CGO/PBCO+CGO cell and the Au gauzes were pressed together physically with spring loading. Electrochemical impedance spectra were obtained using a Solatron 1260 frequency response analyzer. The applied frequency ranges from 2 MHz to 0.01 Hz and operating temperature ranges are $400 \leq T \leq 650\ ^{o}C$. An electrical perturbation (30 mV amplitude) was used throughout the impedance measurements.

The results for the area specific resistance as a function of temperature are shown in Figure 34. At 600 °C the lowest area specific resistance observed was 0.15 ohm-$cm^2$.

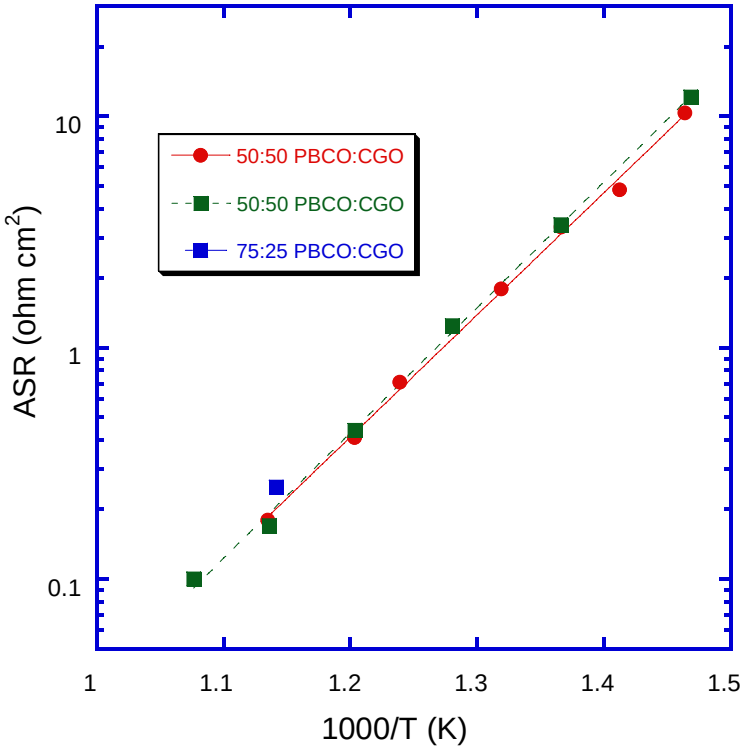


Figure 34. Area Specific Resistances for three symmetric cells PBCO/CGO/PBCO.

### 4.4 Solid oxide fuel cells with $PrBaCo_2O_{5+\delta}$ as cathodes

#### 4.4.1 Fabrication of SOFC with $PrBaCo_2O_{5+\delta}$ as cathodes

The CGO (gadolinium doped ceria) powder was die-pressed into a pellet and sintered at 1450 °C for 8 h in air. The thickness of the CGO electrolyte pellet was reduced to 0.8 mm by polishing with SiC paper. $PrBaCo_2O_{5+x}$ (PBCO) -CGO (50 wt%) was used as the cathode and Ni-CGO (30 vol%) as the anode, respectively. The PBCO-CGO and NiO-CGO pastes were prepared from powder mixtures of PBCO and CGO, NiO and CGO, with the addition of terpineol. The NiO-CGO paste was applied onto the CGO electrolyte and fired at 1300°C for 2 h in air. Then a thin PBCO-CGO green tape (25 μm), which was prepared by tape casting, was stuck to the other side of the CGO electrolyte pellet using terpineol and fired at 1100°C for 30 min in air. The PBCO-CGO paste was subsequently applied onto the surface of the sintered PBCO-CGO tape, and also fired at 1100°C for another 2 h in air to increase the thickness of the cathode. The active electrode area of the cathode and anode was 1.27 $cm^2$. Two pieces of gold mesh were used as current collectors and bonded onto both surfaces of the cathode and anode by firing with gold paste at 700°C for 30 min in air.

#### 4.4.2 Electrical measurements

The electrolyte supported solid oxide fuel cell with the following arrangement was tested from 500°C to 700°C at 25°C intervals:

97 vol% $H_2$ + 3 vol% $H_2O$, Ni-CGO anode / CGO electrolyte / PBCO-CGO cathode, air

The anode side of the single cell was sealed onto an alumina tube with a gold O-ring under spring loading, while the cathode was simply exposed to air. Before testing, the cell was heated to 800 °C to deform the gold O-ring and reduce the NiO to Ni with hydrogen flowing over the anode. The flow rate of the hydrogen fed to the anode was 150 cc/min. Cell current-voltage (I-V) plots were measured using an Arbin Testing System (Model BT 4+). The ohmic resistance of the cell was determined by current interrupt measurements using Keithley SourceMeters.

#### 4.4.3 Results-voltage-current (V-I) characteristics of SOFCs

The voltage-current (V-I) characteristics of the cell are shown in Figure 35. As expected for CGO, the open circuit voltages (OCV) range from 0.87 V at 700 °C to 1.04V at 500 °C and are lower than Nernst potential. The values for the OCV are comparable to those typically measured with ceria-based electrolytes. The decreased OCV is attributed to the increasing contribution of electronic conductivity to the total conductivity as the temperature is increased in a reducing environment.

The power densities as a function of current density from 500 °C to 700 °C are shown in Figure 36. The maximum power densities are ranging from 9.6 $mW/cm^2$ at 500 °C up to 69.4 $mW/cm^2$ at 700 °C. The power densities achievable with this cell are primarily limited by the resistance of the electrolyte. The electrolyte is 0.8 mm thick and contributes the major part of the total cell resistance above 500 °C. The total ohmic resistance of the cell was determined using the current interruption technique. The results are compared with the calculated resistance of CGO using literature data.

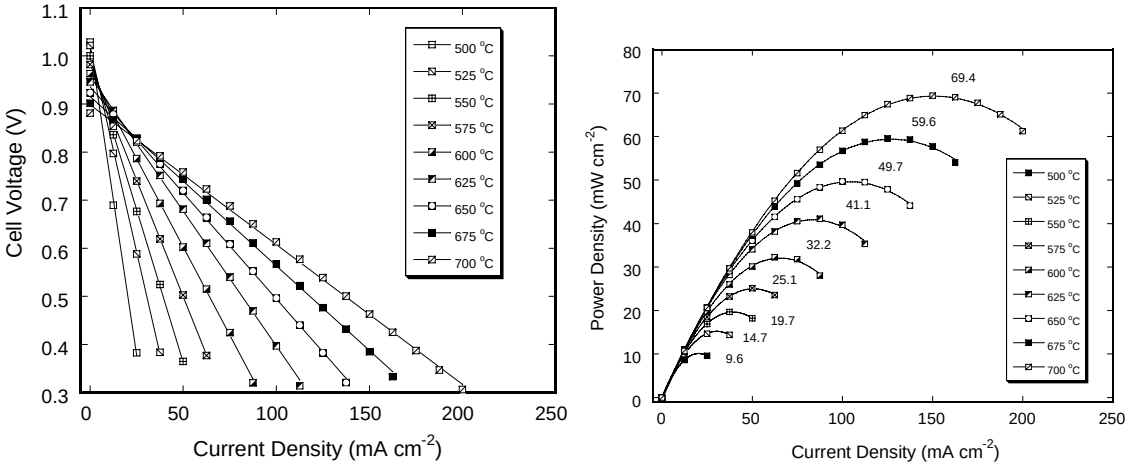


Figure 35. V-I characteristics and power densities as a function of current density of the CGO electrolyte supported solid oxide fuel cell with a PBCO cathode.

At 700 °C the ohmic resistance of the cell is effectively equal to that of the electrolyte. At 600 °C the difference is small (0.27 ohms) and increases to 5.4 ohms at 500 °C. The present experimental data do not enable the specific electrode contributions to be isolated. Nevertheless at 600 °C the data indicate low electrode resistances.

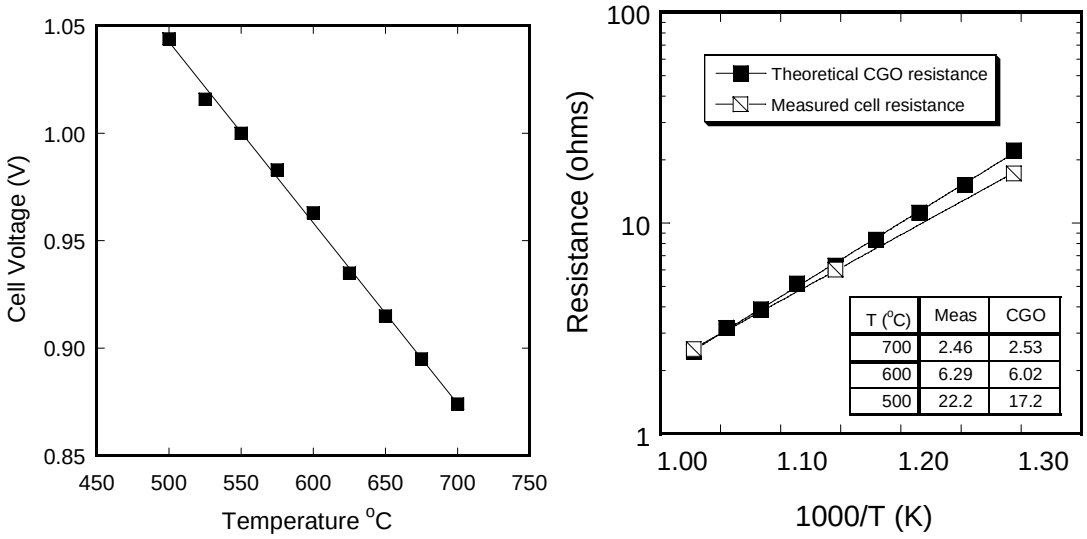


Figure 36. Open circuit voltages (left) and a comparison of the ohmic resistance of the cell measured by current interrupt technique and the calculated theoretical resistance of the electrolyte.

### 4.5 Thin films of $PrBaCo_2O_{5+\delta}$ (PBCO) on $SrTiO_3$ (STO)

#### 4.5.1 Synthesis of Thin films of $PrBaCo_2O_{5+\delta}$ (PBCO) on $SrTiO_3$ (STO)

A pellet of $PrBaCo_2O_{5+\delta}$ (PBCO) of 1" diameter was pressed from the powder and then sintered in air at 1100 ºC for 10 h to serve as the target for pulsed laser deposition (PLD). The pellet was shown to be single phase by powder X-ray. Thin films of PBCO were

deposited on (001) oriented $SrTiO_3$ (STO) single crystal substrates because of their excellent lattice matching. The typical PBCO film thickness is about ~1500Å. Samples were rectangular with dimensions 10 mm × 3 mm.

### 4.5.2 Characterization of Thin films of $PrBaCo_2O_{5+\delta}$ (PBCO)

The PBCO films were characterized by X-ray diffraction using the z-axis diffractometer at the NSLS, beamline X22C. The wavelength used was 1.5406 Å. In the grazing incidence geometry, the incident angle was selected by rotating the diffractometer against the incoming beam and the exit angle was defined to be the same as the incident angle by a pair of slits. Figure 37 shows radial scans along the STO [200] in-plane direction using different scattering depths Λ. In addition to the PBCO (004) reflection ($c_{PBCO}$ = 7.727 Å), the PBCO(200) ($a_{PBCO}$ = 3.908 Å) peak is superimposed on the STO(200) ($a_{STO}$ = 3.905 Å). The rocking curve (width in θ) of the PBCO(002) reflection has only a full width half maximum of 0.1 deg, compared to a resolution-limited width of the STO(002) of 0.007 deg, indicating that the as-grown PBCO thin films on (001) STO have excellent single crystallinity and epitaxial behavior. Upon increasing Λ, an interfacial peak at 2θ = 41.2 deg becomes visible. This interfacial phase exhibits a much smaller coherence length (160 Å) than the remainder of the film. The interface relationship was determined from this scan and corresponding out-of-plane scans to be [001], $[100]_{PBCO}$//$[100]_{STO}$ and $[010]_{PBCO}$ // $[001]_{STO}$.

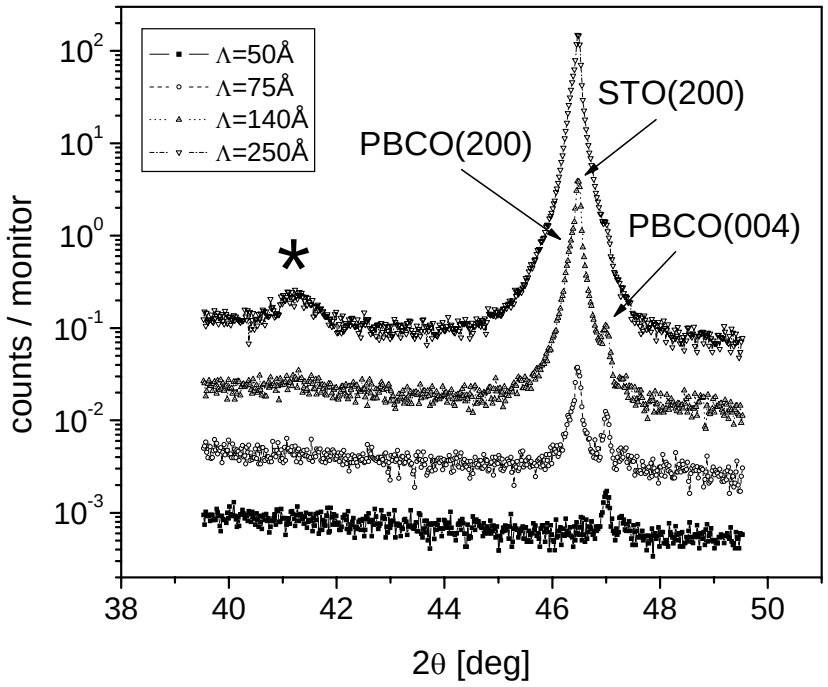


Figure 37. Grazing incidence diffraction scans along the substrate's [200] direction for different scattering depths. The curves are shifted for clarity. Labeling of the PBCO peaks is according to the Pmmm structure. The asterisk marks an (unknown) interfacial phase.

### 4.4.3 DC Conductivity of Thin films of $PrBaCo_2O_{5+\delta}$ (PBCO)

The electrical conductivities of PBCO films on STO substrates in air were measured to determine the high temperature transport properties. As the temperature is increased,

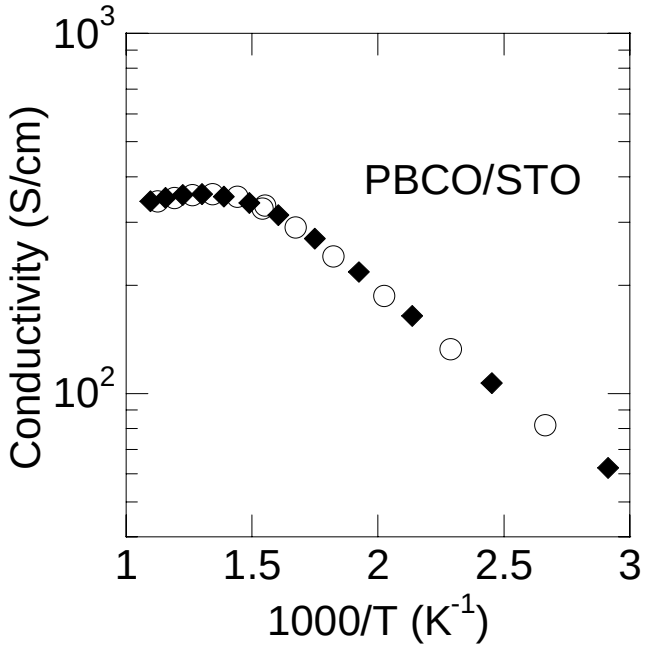


Figure 38. Conductivity of a PBCO film in air. Solid and open symbols correspond to measurements made on increasing and decreasing temperature, respectively.

the conductivity first increases due to thermal activation and then falls as the film starts to lose oxygen with an accompanying decrease in the hole concentration (Figure 38). The transition point is near 645 K. It is important to note that the PBCO films on (001) STO have excellent electrical conductivity, ~ $10^2$ S/cm$^2$, over a very broad temperature region of 300 to 1000 K. Compared with the traditional electrode materials such as $(La,Sr)MnO_3$ or $(La,Sr)(Co,Fe)O_3$, PBCO thin films have much better electrical conductivity especially in the low temperature region.

### 4.4.4 ECR Studies of Thin films of $PrBaCo_2O_{5+\delta}$ (PBCO)

The oxygen transport kinetics in the PBCO films were determined by electrical conductivity relaxation (ECR) and isotope exchange and depth profiling (IEDP) in various oxygen environments. In ECR experiments, the sample is first held at equilibrium at an initial oxygen partial pressure. Then at constant temperature, the gas atmosphere is changed abruptly to a new oxygen pressure. The change in the conductivity of the sample, which reflects the change in the oxygen content, is recorded until the new equilibrium is established. By analyzing the normalized conductivity,

$$g(t) = (\sigma_t - \sigma_0)/(\sigma_\infty - \sigma_0)$$

where $\sigma_0$ and $\sigma_\infty$ are the initial and final conductivity, respectively, the chemical diffusion coefficient, $\tilde{D}$, and the chemical surface exchange coefficient, $k_{chem}$ can be

directly obtained. Since the as-grown PBCO film is very thin (<2000 Å), it is reasonable to assume that the oxygen transport is controlled by the surface exchange rate. For a single surface reaction, the normalized conductivity of a plate sample is $g(t) = 1 - \exp(-t/\tau)$ where $\tau$ is the time constant.

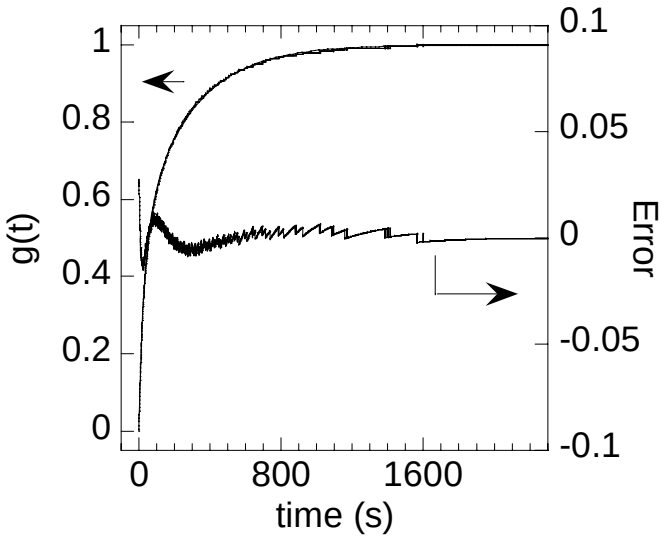


Figure 39. Representative conductivity relaxation data for PBCO/STO at 430 ºC. The gas switch was from 5% to 1% $O_2$. $A_1 = 0.48$, $A_2 = 0.49$, $\tau_1 = 34.5$ s, $\tau_2 = 284$ s. The error axis indicates differences between the experimental data and the fit.

The experimental data are not well described by this simple model but a good fit can be obtained using two independent time constants according to $g(t) = 1 - A_1 \exp(-t/\tau_1) - A_2 \exp(-t/\tau_2)$ with $A_1 + A_2 = 1$ and $\tau_1$ and $\tau_2$ are the time constants. This kinetic model implies that the PBCO film consists of two independent regions with different exchange rates that could correspond to two different film microstructures or to reactions on the highly epitaxial film and the surface step terrace induced antiphase domain boundaries.[2]

A typical fit to the ECR data for a PBCO/STO film is shown in Figure 39. The good agreement confirms the assumption that the kinetics are surface controlled. The surface exchange coefficients calculated from the two time constants ($k_{chem,n} = l/\tau_n$, $l$ is the thickness of the film). As we can see, $k_{chem,1}$ is one order of magnitude higher than $k_{chem,2}$, suggesting two distinct kinetics region exist. In both regions, oxidation (low pressure to high pressure) is faster than reduction (high pressure to low pressure), as usually observed for the surface exchange reaction.[3]

### 4.4.5 Isotope Exchange and Depth Profiling of Thin Films of $PrBaCo_2O_{5+\delta}$ (PBCO).

The surface exchange rate was determined for a PBCO/STO film sample by isotope exchange and depth profiling. The sample was exposed to $^{18}O$ at 0.2 atm at 500 ºC for 700 s and then rapidly quenched. The $^{18}O$ profile in the sample was then analyzed by ToFSIMS using an ION-TOF IV with Ga gun. The sample was sputtered with $Cs^+$ at

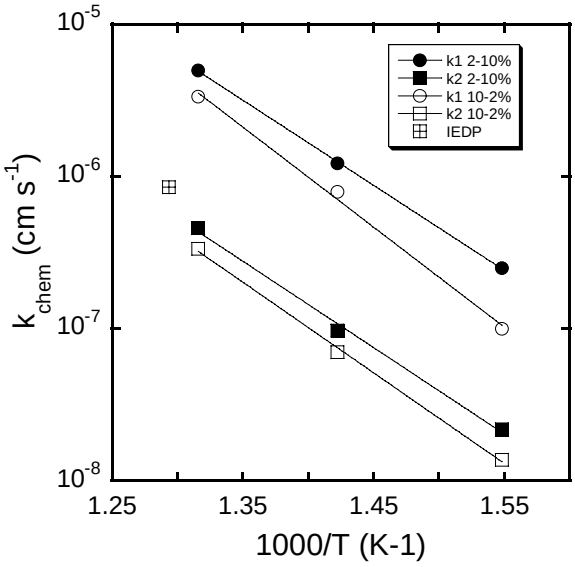


Figure 40. The surface exchange coefficients measured for PBCO/STO. The filled symbols correspond to a gas switch from 0.02 to 0.1 atm and the open symbols from 0.1 to 0.02 atm. The cross hatched square is the IEDP measurement.

20keV in “burst" mode (multiple primary ion pulses) to avoid saturation in the $^{16}O$ signal. The profile was the fitted to obtain the surface exchange coefficient and the oxygen diffusion coefficient in the STO. The experiment confirms that the oxygen diffusion in the film is too fast to be measured. The relationship between the surface exchange coefficient determined by the IEDP and ECR techniques is $k_{chem}$ (ECR) / $\Gamma$= $k_O$ (IEDP) where $\Gamma$ is the thermodynamic factor ($\Gamma = d\mu_O/dc_O$ where $\mu_O$ and $c_O$ are the oxygen chemical potential and concentration, respectively). In order to compare the IEDP measurement with the ECR data, we have assumed the $\Gamma$ value previously measured for bulk material.[6] Data from both ECR and the IEDP measurement are shown in Figure 40.

### 4.4.6 Additional Isotope Exchange and Depth Profiling of Thin Films of $PrBaCo_2O_{5+\delta}$ (PBCO).

In a continuation of the thin film studies of $PrBaCo_2O_{5+x}$ the surface exchange rate and interface transfer rates were determined for a PBCO/CGO/YSZ film sample by isotope exchange and depth profiling. The sample was prepared by pulsed laser deposition on a single crystal of YSZ. Initially half the sample was masked and CGO deposited and then PBCO deposited over the whole sample to give the structure shown schematically below.

The sample was exposed to $^{18}O$ at 0.2 atm at 700 ºC for 120 s and then rapidly quenched. The $^{18}O$ profile in both regions of the sample was then analyzed by ToFSIMS using an ION-TOF IV with Ga gun. The sample was sputtered with $Cs^+$ at 20keV in “burst" mode (multiple primary ion pulses) to avoid saturation in the $^{16}O$ signal. The surface exchange coefficient was determined from the oxygen concentration.

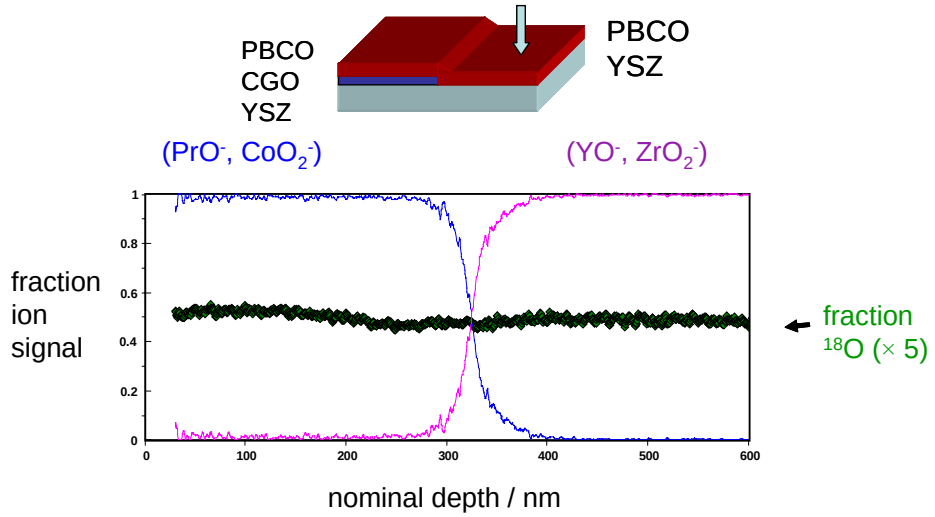


Figure 41. Depth Profile of PBCO/YSZ.

The ion signals from the PBCO layer ($PrO^-$ and $CoO_2^-$) and from YSZ ($YO^-$ and $ZrO_2^-$) are shown in Figure 41 and indicate a sharp interface. The fraction of 18O is uniform across the film and the PBCO/YSZ interface. The fall off into the YSZ itself is not apparent on this length scale. Similar results were obtained for the PBCO/CGO/YSZ profile show in Figure 42. Under these conditions, no resistance to oxygen transfer is observed.

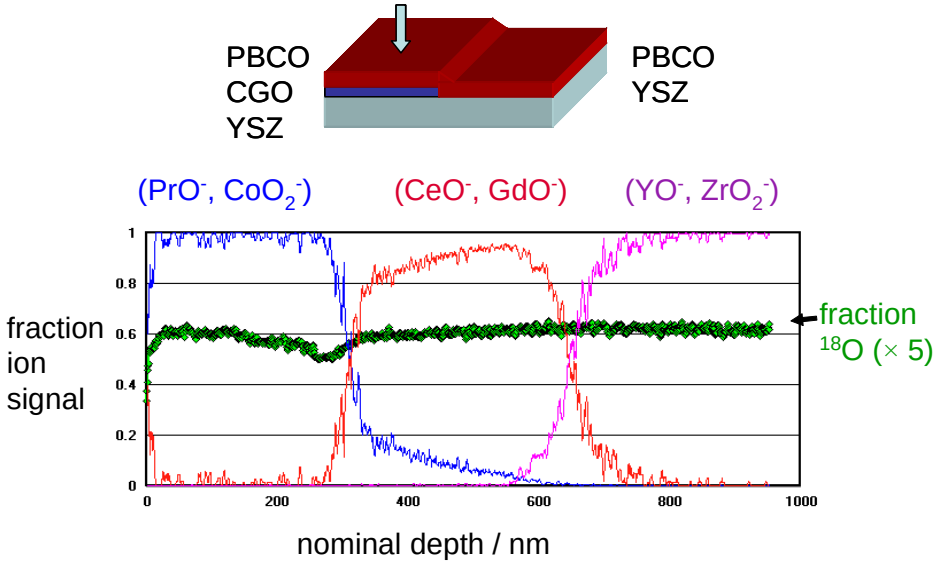


Figure 42. Depth Profile of PBCO/CGO/YSZ

The surface exchange coefficient determined from these measurements, the earlier results on STO and the ECR thin film measurements are summarized in Figure 43 and are all in reasonable agreement.

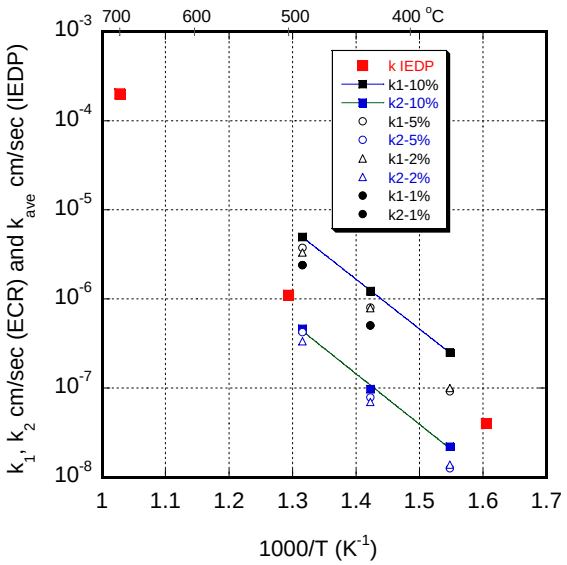


Figure 43. Comparison of the IEDP and ECR measurements of the surface exchange coefficients of PBCO films

### 4.6 Combinatorial Approach to Measurement of Transport Parameters.

Perovskite and perovskite related oxides are noteworthy for their tolerance of a very wide range of compositions. This is an advantage in that variations in composition can be used to simultaneously optimize several important properties such as surface exchange rate, diffusion coefficient, thermal expansion, and substrate reactivity. The disadvantage is that the matrix of possible compositions is very large and serial evaluation of properties is time consuming. Consequently, we have decided to adopt a combinatorial approach whereby many compositions can be screened for one or more properties using a single specimen. The $LaFeO_3$ – $SrFeO_{2.5}$ system has been shown recently to be of interest as cathode materials for intermediate temperature operation and was selected in this study. Samples were prepared in the form of thin films by pulsed laser deposition (PLD) on single crystal yttria stabilized zirconia substrates. The general approach is shown in Figure 44.

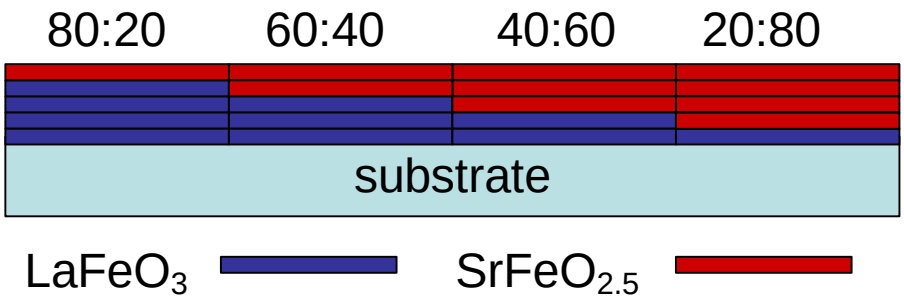


Figure 44. Schematic of the Approach to Make Multiple Compositions on One Substrate.

A shadow mask was used to deposit the first oxide ($LaFeO_3$ in Figure 44) in steps of different thickness. In a second step, the second oxide ($SrFeO_{2.5}$ in Figure 44) was deposited in reverse order to produce a film of uniform total thickness. The films were deposited with the substrate at ambient temperature where they were amorphous.

Subsequent annealing was used to interdiffuse the two compositions and to crystallize the materials. The total film thickness is typically of the order of 3000 to 5000 Å on substrates 1cm × 1cm. Consequently vertical interdiffusion is much faster than lateral diffusion and the compositional differences will be maintained.

### 4.6.1 Synthesis of Laser Deposition Targets.

$LaFeO_3$ was synthesized using a precursor method. Equimolar amounts of $La(NO_3)\cdot 6H_2O$ and $K_3Fe(CN)_6$ aqueous solutions were mixed with continuous stirring to form reddish-orange $LaFe(CN)_6\cdot 5H_2O$ as a precipitate. The precursor was washed using water and ethyl alcohol. After drying at 50 °C, the precursor was decomposed at 1000 °C for 4 h and then 1200 °C for 5 h. X-ray powder diffraction was used to confirm that the product was single phase $LaFeO_3$.

$SrFeO_{3-\delta}$ was synthesized using a conventional solid state reaction method. A stoichiometric ratio of preheated (150 $^oC$, overnight) $SrCO_3$ (Alfa-Aesar, 99.99%) and $Fe_2O_3$ (Aldrich, 99.998%) were mixed in a mortar and pestle in ethyl alcohol and then heated at 1000 °C for 5h. The resulting black powder was ball-milled in ethyl alcohol with $ZrO_2$ balls for 24 h.

To make the targets for pulsed laser deposition, powders of $LaFeO_3$ and $SrFeO_{3-\delta}$ were pressed uniaxially into green disks of 1" diameter and 7 mm thickness. The green disks of $LaFeO_3$ and $SrFeO_{3-\delta}$ were sintered at 1250 °C for 5 h and 1350 $^oC$ for 12 h, respectively.

### 4.6.2 Deposition and Crystallization of Amorphous Films of $LaFeO_3$ and $SrFeO_{2.5}$.

Amorphous films of $LaFeO_3$ and $SrFeO_{2.5}$ were deposited on (001) MgO substrates by pulsed laser ablation at room temperature in an atmosphere of 200 mTorr oxygen with stoichiometric targets. To determine the appropriate annealing procedure, we measured the resistance of films of both compounds as a function of temperature, since in general electrical transport properties reflects micro-structural characteristics of complex transition metal oxides. On the other hand, this method is faster and reveals more accurate information than using XRD alone because some transitions may occur at temperatures only a few degrees apart. The resistances of the films were measured e in 1 atm $O_2$ using the 4-probe technique. Four platinum leads of 0.001 in. diameter were mechanically mounted onto the film directly to serve as current and voltage electrodes. No conductive glue was used to avoid experimental artifacts from possible reaction between conductive glue and the amorphous films. Current was provided by using a Keithley 2400 sourcemeter and was continuously adjusted during the measurement according to the resistance of the films. The voltage was measured using a Keithley 2000 multimeter. Films were slowly heated a rate of 1 °C/min. Six data points were collected for every degree increase so that fine features of the dynamics of crystallization and phase transitions were not missed.

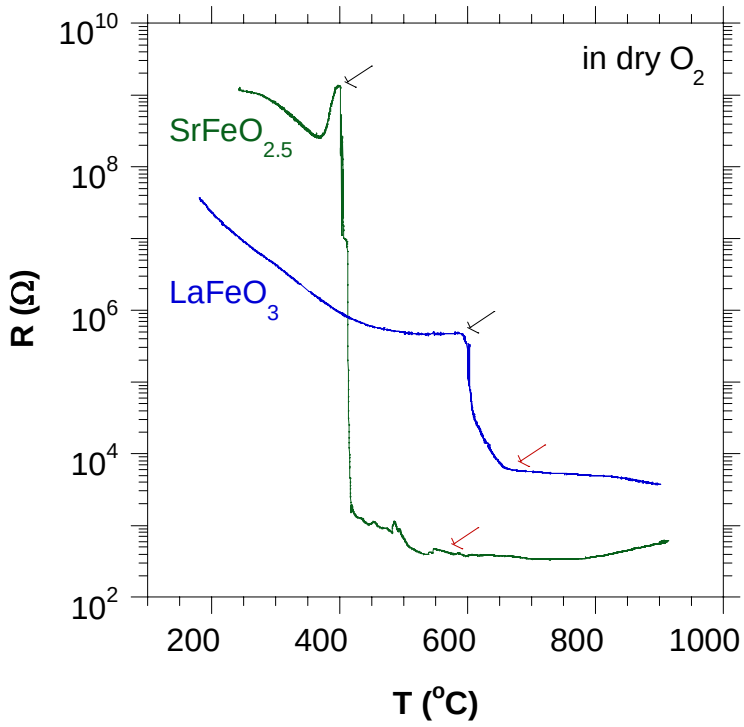


Figure 45. Temperature dependence of the resistance of amorphous $SrFeO_{2.5}$ and $LaFeO_3$ films.

The resistance of both amorphous $SrFeO_{2.5}$ film and $LaFeO_3$ film in dry oxygen is plotted as a function of temperature in Figure 45.

The nucleation and crystallization process, characterized by a sharp drop in resistance, started at about 400 °C and 600 °C for $SrFeO_{2.5}$ film and $LaFeO_3$ film, respectively (shown by the black arrows). It was complete at about 550 °C for the $SrFeO_{2.5}$ film and 650 °C for the $LaFeO_3$ film, shown by the red arrows. These results suggest the following annealing procedure for the composite films of $SrFeO_{2.5}$ /$LaFeO_3$ : first anneal the films at temperatures lower than 400 °C for an appropriate period time to interdiffuse the two compositions, and then anneal them at temperatures higher than 650 °C to ensure the complete crystallization of the composite films.

### 4.6.3 Interdiffusion of Amorphous Bilayer Films of $LaFeO_3$ and $SrFeO_{2.5}$.

Our first goal is to make combinatorial thin films in the $LaFeO_3$ – $SrFeO_{2.5}$ system. This requires the interdiffusion of amorphous films of two separate compositions. Two types of amorphous films, $LaFeO_3$ on $SrFeO_{2.5}$ ($LaFeO_3$/$SrFeO_{3-d}$ ) and the reverse ($SrFeO_{3-d}$/$LaFeO_3$), were deposited on $LaAlO_3$ (LAO) substrates. The deposition method was the same as described previously. The specific procedure used to treat the films was a two-step heat treatment in $O_2$, first at 380°C for 110 h and then 715 °C for 8h.

XRD patterns of the annealed films are shown in Figures 46 (a) and (b). The two large peaks (2θ at 24° and 48°) are from the LAO substrate (001) and (002) diffraction lines. For $SrFeO_{3-\delta}$/$LaFeO_3$ film (Figure 46 (a)), the film peaks can be indexed as from the powder $SrFeO_{2.5}$ (17-0932), indicating that the film is not oriented.

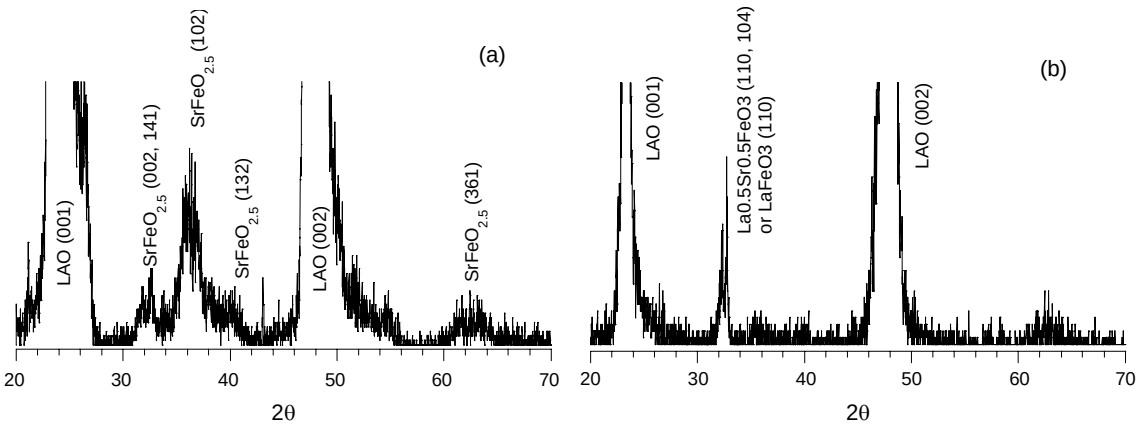


Figure 46. XRD spectra of annealed thin films on LAO substrate, a) $SrFeO_3/LaFeO_3$ b) $LaFeO_3/SrFeO_3$, after heated in $O_2$ at 380 $^oC$ for 110 h and followed by 715 $^oC$ for 8 h**.**

For $LaFeO_3/SrFeO_{3-d}$ film (Figure 46 (b)), we see only one peak, indicating that the film is oriented. The peak at 32.7$^o$ could be either from the $LaFeO_3$ (110) diffraction line (75-0439) or from the $La_{0.5}Sr_{0.5}FeO_3$ (110) and (104) lines (82-1962). If it is the latter, the heat treatment succeeded in interdiffusing the two compositions. The $LaFeO_3$ / $SrFeO_3$ sample was then further examined by SIMS to determine the extent of interdiffusion.

### 4.6.4 Surface Analysis of $LaFeO_3$ / $SrFeO_3$ on LAO

A survey scan was performed to determine the mass of the most intense elements sputtered from the two layer sample. Initially a negative ion scan was performed in the hope of increasing the sensitivity. The intensity of metal oxides in a negative ion scan is generally greater than in a positive ion scan. Charge build up, however, limits the sensitivity even with charge neutralization and mass 88 is obtained from Sr as well as from $FeO_2$. Consequently, a positive $Ga^+$ survey scan was performed. In this case the mass of each element is selected. Interestingly LaO of mass 155 amu appears in the positive ion scan and was monitored also. Ga was also monitored to confirm the separation of the layers and to check for matrix effects. The masses monitored were $^{16}O$, $^{27}Al$, $^{69}Ga$, $^{56}Fe$, $^{88}Sr$, $^{139}La$, and $^{155}$(LaO).

A $Ga^+$ depth profile was performed at 5000 times normal magnification at 60 deg to the sample normal at 25 kV incident energy with charge neutralization throughout. The depth profile is shown in Figure 47. From left to right, the $LaFeO_3$ top layer, the $SrFeO_3$ layer, and the lanthanum aluminate (LAO) substrate are observed. The Fe intensity and thus concentration appear constant in the first two layers, as expected from the stoichiometry. The Al intensity is very low and is also constant in the first two layers and is attributed to background noise indicating that Al diffusion is negligible. The Ga intensity in the first two layers is constant indicating that matrix effects are not of concern. In the first region, the La intensity is high and then decreases to background noise in the second region indicating that the first layer is $LaFeO_3$ and that some La diffusion into the second layer has occurred. In the first region, the Sr intensity is low but is above the background noise level. The Sr intensity rises sharply to a high constant value in the second region. The second layer is $SrFeO_{3-x}$ and Sr diffusion into the first layer occurs to a greater extent

than the La diffusion in the reverse direction. The third region is indicated by an abrupt drop in intensity of all masses and is a result of the highly insulating nature of LAO.

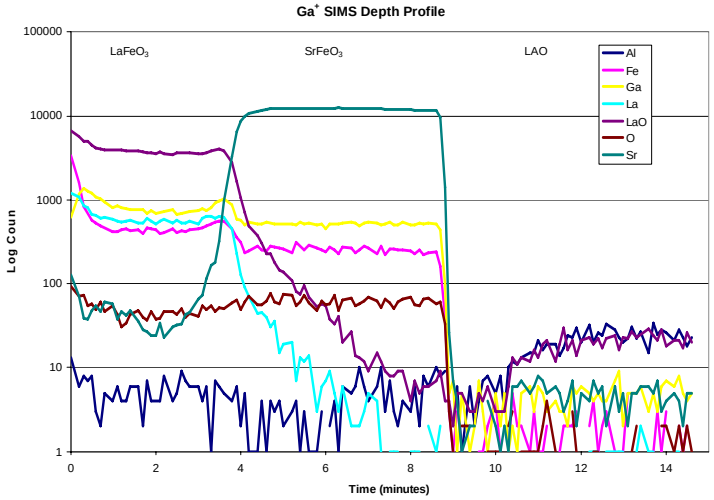


Figure 47. $Ga^+$ SIMS depth profile of $LaFeO_3$ on $SrFeO_3$ on a LAO substrate.

Profilometer measurements do not give a crater depth from the depth profile because of the roughness of the sample surface. Thus, the sputter rates are not yet determined and the sputter depth is not known. Smooth single samples of each layer will be sputtered at the same magnification to determine these rates. The origin of the surface roughness will also be further investigated.

### 4.6.5 Laser Deposition of (La,Sr)$FeO_{3-x}$ Samples:

We prepared a number of different film geometries with 2, 4, and 8 layers in sequences starting with either $LaFeO_3$ or $SrFeO_{2.5}$ as the first layer deposited on the substrate using pulsed laser deposition (PLD). The deposition method was described previously. All films were deposited at ambient temperature and subsequently annealed at two different temperatures as indicated in the summary table below (Table 4). The total film thickness was ~3000 Å in each case. The samples were analyzed by X-ray diffraction after annealing and then depth profiled using SIMS and a gallium ion source to determine the extent of inter-diffusion.

The most successful processing conditions to date were obtained for a 4-layer film, $SrFeO_{2.5}/LaFeO_3/ SrFeO_{2.5}/LaFeO_3/LaAlO_3$ (Sr/La/Sr/La/LaO) (#8 in Table 4). For inter-diffusion, the film was heated at 504 °C for 113 h and then 703 °C for 10 h in flowing oxygen. The annealing temperature was increased relative to the earlier experiments from 380 °C to 500 °C to accelerate the inter-diffusion process. This temperature is above the crystallization temperature of $SrFeO_{2.5}$ (400 °C) but below the crystallization temperature of $LaFeO_3$ (600 °C).

The XRD pattern of the annealed film is shown in Figure 48. The film has some orientation with respect to the substrate as indicated by the two large $La_{0.5}Sr_{0.5}FeO_3$ peaks at 22.7 (001) and 46.4° (002). The peak at 27.2 ° is possibly from $LaFeAl_{11}O_{19}$ formed by reaction between the $LaFeO_3$ layer and the $LaAlO_3$ substrate. The small peaks at 32.4-

32.8 $^{o}$ and 39.9 $^{o}$ are most likely due to (110) and (111) reflections from other film orientations.

Table 4. Thin film samples and annealing conditions

| | XRD | SIMS | Sample | layers | 1st annealing | | 2nd annealing | |
|---|---|---|---|---|---|---|---|---|
| | | | | | T & t | Atm. | T & t | Atm. |
| 1 | √ | x | $SrFeO_{2.5}/LaFeO_3/LAO$ | 2 | 380$^{o}$C, 110h | $O_2$ | 714 $^{o}$C, 8h | $O_2$ |
| 2 | √ | √ | $LaFeO_3/SrFeO_{2.5}/LAO$ | 2 | 380$^{o}$C, 110h | $O_2$ | 714 $^{o}$C, 8h | $O_2$ |
| 3 | √ | √ | $LaFeO_3/SrFeO_{2.5}/LAO$ | 2 | 350 $^{o}$C, 50 h | $O_2$ | 703 $^{o}$C, 15h | $O_2$ |
| 4 | √ | √ | $LaFeO_3/SrFeO_{2.5}/LAO$ | 2 | 350 $^{o}$C, 167 h | $O_2$ | 703 $^{o}$C, 15h | $O_2$ |
| 5 | √ | √ | $LaFeO_3/SrFeO_{2.5}/LAO$ | 4 | 350 $^{o}$C, 171 h | $O_2$ | 703 $^{o}$C, 10h | $O_2$ |
| 6 | √ | √ | $SrFeO_{2.5}/LaFeO_3/LAO$ | 2 | 350 $^{o}$C, 171 h | $O_2$ | 703 $^{o}$C, 10h | $O_2$ |
| 7 | √ | √ | $SrFeO_{2.5}/LaFeO_3/LAO$ | 2 | 504 $^{o}$C, 113 h | $O_2$ | 703 $^{o}$C, 10h | $O_2$ |
| 8 | √ | √ | $SrFeO_{2.5}/LaFeO_3/LAO$ | 4 | 504 $^{o}$C, 113 h | $O_2$ | 703 $^{o}$C, 10h | $O_2$ |
| 9 | √ | √ | $SrFeO_{2.5}/LaFeO_3/LAO$ | 8 | 504 $^{o}$C, 278 h | air | 703 $^{o}$C, 10h | air |
| 10 | √ | x | $SrFeO_{2.5}/LaFeO_3/LAO$ | 8 | 504 $^{o}$C, 278 h | air | 703 $^{o}$C, 10h | air |
| 11 | √ | x | $SrFeO_{2.5}/LaFeO_3/LAO$ | 4 | 504 $^{o}$C, 278 h | air | 703 $^{o}$C, 10h | air |
| 12 | √ | x | $SrFeO_{2.5}/LaFeO_3/LAO$ | 4 | 504 $^{o}$C, 278 h | air | 703 $^{o}$C, 10h | air |
| 13 | √ | x | $SrFeO_{2.5}/LaFeO_3/LAO$ | 2 | 504 $^{o}$C, 278 h | air | 703 $^{o}$C, 10h | air |

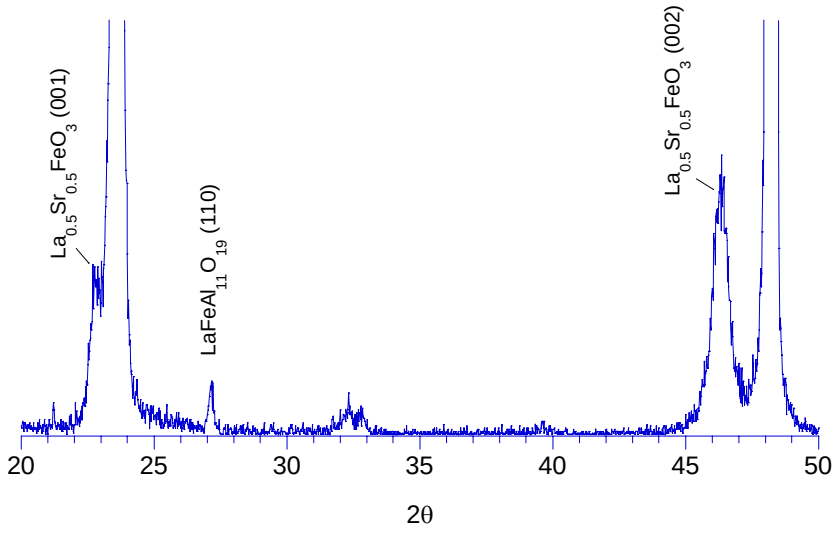


Figure 48. XRD pattern of an annealed 4-layer Sr/La/Sr/La thin film after heating in air at 500 $^{o}$C 113h and then 700 $^{o}$C for 10h.

The SIMS data are consistent with the X-ray result and indicate substantial though not quite complete inter-diffusion. Although we have demonstrated a processing approach to synthesize $La_{0.5}Sr_{0.5}FeO_3$ from the components, the slow interdiffusion rates and the difficulty of obtaining homogeneous compositions led us to discontinue this part of the project.

### 4.7 Ink jet printing of oxide patterns:

A commercial piezo-electric ink-jet printer (3 color + black) has been modified to deposit patterned oxide layers on single crystal and ceramic substrates. The method will be used to generate patterns to test the roles of surfaces and phase boundaries (double and triple) in the activation and transport of oxygen by isotope methods. The composition of the printed pattern is governed by a custom-written printer driver which was written from scratch to avoid the color correction that is normally done by commercial printer drivers. Also the printer feed mechanism was also modified to allow flat, thin solid samples to be fed through the paper path.

The research has focused on optimization of the deposition system for the combinatorial samples, using inorganic solutions plus polyethylene glycol (PEG) to optimize the drying of the printed specimen. The printed samples are then dried and calcined. Initial problems of nozzle clogging were solved by optimization of the PEG concentration. The initial materials involved the printing of (Gd + Ce) solutions onto single crystal (100) YSZ specimens. Specimens with a programmed variation in the Gd/Ce ratio have been prepared. These samples were characterized by SEM, ToFSIMS, and XPS at a variety of annealing conditions. This work was not completed

## 5. Conclusions

We have adopted a combinatorial approach, initially with the $LaFeO_3 – SrFeO_{2.5}$ system for study of transport kinetics. We have also synthesized and measured the DC conductivity of two examples of P1 compositions $La_{0.7}Sr_{0.3}FeO_3$ and $La_{0.8}Sr_{0.2}FeO_3$ and characterized the surface chemistry.

We have prepared single phase samples of $La_xPr_{2-x}NiO_{4+d}$ (x =2.0, 1.9, 1.5, 1.2, 1.0, 0.5 and 0) and obtained their oxygen ion diffusion coefficients and the surface exchange coefficients extracted. We have evaluated the performance of $Ln_2NiO_{4+d}$, Ln =La, Pr, in symmetric cells. Reactivity studies indicated evidence for significant reaction with YSZ and so the data were collected on gadolinium doped ceria electrolytes. The area specific resistances are low enough to warrant further studies

The oxygen exchange kinetics of the oxygen deficient double perovskite $LnBaCo_2O_{5.5+x}$ (Ln = Pr and Nd) have been determined by electrical conductivity relaxation. The high electronic conductivity and rapid diffusion and surface exchange kinetics of $PrBaCo_2O_{5.5+\delta}$ suggest its application as cathode material in intermediate temperature solid oxide fuel cells. Preliminary measurements show low ASR values at 600 °C. This led to the extended measurements on complete cells and we describe here the results that we have obtained for electrolyte supported cells

The oxygen exchange kinetics of highly epitaxial thin films of the oxygen deficient double perovskite $PrBaCo_2O_{5.5+\delta}$ (PBCO) have been determined by electrical conductivity relaxation and isotope exchange and depth profiling. The thin films of $PrBaCo_2O_{5.5+\delta}$ were prepared by pulsed laser deposition (PLD) on single crystal substrates. The electrical conductivity relaxation (ECR) and isotope measurements agree well though the ECR data indicate the presence of two distinct kinetic pathways. Isotope exchange and depth profiling of thin film structures on both YSZ and CGO show little or no barrier to interfacial transport.

A commercial piezo-electric ink-jet printer has been modified to deposit patterned oxide layers on single crystal and ceramic substrates. The method will be used to generate patterns to test the roles of surfaces and phase boundaries (double and triple) in the activation and transport of oxygen by isotope methods.

We have also investigated the possibility of substituting cerium for either lanthanum or praseodymium. This is not successful and even at small doping levels a second fluorite phase is apparent. This suggests that these materials will be compatible with CGO. The phase compatibility of $La_2NiO_4$, $Pr_2NiO_4$ and $PrBaCo_2O_{5.5+x}$ with YSZ and GDC electrolytes was investigated by solid state reaction and powder X-ray diffraction. PBCO is found to be compatible with CGO.

Overall, we have successfully finished the project with outstanding results particularly with respect to the discovery of the remarkable properties of A site ordered perovskites.

## 6. References


1. *Electrochemical Intercalation of Oxygen in $La_2NiO_{4+x}$: Phase Separation Below Room Temperature*, Yazdi, I.; Bhavaraju, S.; DiCarlo, J. F.; Scarfe, D. P.; Jacobson, A. J., Chem. Mater. (1994) *6* 2078-2084.
2. *Electrochemical Intercalation of Oxygen in $Nd_2NiO_{4+x}$ ($0 \leq x \leq 0.18$) at 298K*, Bhavaraju, S.; Di Carlo, J. F.; Scarfe, D. P.; Yazdi, I.; Jacobson, A. J., Chem. Mater. (1994) *6* 2172-2176.
3. *Oxygen diffusion & surface exchange in $La_{2-x}Sr_xNiO_{4+x}$*, Skinner, S.J.; Kilner, J.A., Solid State Ionics (2000) *135* 709-712.
4. *Oxygen diffusion and surface exchange in the mixed conducting perovskite $La_{0.6}Sr_{0.4}Fe_{0.8}Co_{0.2}O_{3-x}$*, Benson, S. J.; Chater, R.J.; Kilner, J. A. Proc. Electrochem. Soc. (1998) *1997-24* 596-609.
5. *Ionic transport in oxygen-hyperstoichiometric phases with $K_2NiF_4$-type structure,* Kharton, V. V.; Viskup, A. P.; Kovalevsky, A. V.; Naumovich, E. N.; Marques, F. M. B., Solid State Ionics (2001) *143* 337-353.
6. *Transport and Permeation Properties of $La_2NiO_{4+x}$*, Tichy, R.S.; Huang, K. Q.; Goodenough, J. B.; Proc. Electrochem. Soc. (2001) *2000-32* 171.
7. *Structure and properties of the Nickel (III) Oxide Family: $LnSr_5Ni_3O_{11}$*, James, M.; Attfield, J. P.; Rodriguez-Carvajal, J., Chem. Mater. (1995) *7* 1448.
8. *Synthesis, Structure, and Properties of a Novel Metallic Nickel (III) Oxide, $CeSr_7Ni_4O_{15}$*, James, M.; Attfield, J. P., *Chem. Mater.* (1995) *7* 2338.
9. *Nonstoichiometric $K_2NiF_4$ Type Phases in the Lanthanum Cobalt Oxygen System*, Lewandowski, J. T.; Beyerlein, R. A.; Longo, J. M.; McCauley, R. A., J. Amer. Ceram. Soc. (1986) *69* 699-703.
10. *An Electrical Conductivity Relaxation Study of $La_{0.6}Sr_{0.4}Fe_{0.8}Co_{0.2}O_{3-x}$,* Wang, S.; van der Heide, P. A. W.; Chavez, C.; Jacobson, A. J.; Adler, S. B. *Solid State Ionics* (2003) *156* 201-208.
11. *YSZ – Supported Cathodes of Rare Earth Nickelates $Ln_2NiO_{4+x}$ For ITSOFC (650 °C)*, Bassat, J. M.; Boehm, E.; Grenier, J. C.; Mauvy, F.; Dordor, P.; Pouchard, M., *Fifth*

*European Solid State Fuel Cell Forum*, (2002) 586-593.

## 7. List of Acronyms and Abbreviations

| | |
|---|---|
| CGO | Cerium Gadolinium Oxide |
| ECR | Electrical Conductivity Relaxation |
| EPMA | Electron Probe MicroAnalysis |
| GDC | Gadolinia Doped Ceria (see CGO) |
| LSGM | Lanthanum Strontium Magnesium Gallate |
| PLD | Pulsed Laser Deposition |
| TGA | Thermogravimetric Analysis |
| YSZ | Yttria Stabilized Zirconia |
| IEDP | Isotope Exchange and Depth Profiling |
| PBCO | Praesodymium Barium Cobalt Oxide |
| STO | Strontium Titanate |
| LAO | Lanthanum Aluminate |

## 8. Publications

1. Yoo, Jiho; Verma, Atul; Wang, Shuangyan; Jacobson, Allan J. "Oxygen transport kinetics in $SrFeO_{3-x}$, $La_{0.5}Sr_{0.5}FeO_{3-x}$, and $La_{0.2}Sr_{0.8}Cr_{0.2}Fe_{0.8}O_{3-x}$ measured by electrical conductivity relaxation." J. Electrochem. Soc. **2005** *152* A497-A505.
2. Kim, G. Wang, S. Jacobson, A. J. Yuan, Z. Donner, W. Chen, C. L. Reimus, L. Brodersen, P. and Mims, C. A. "Oxygen exchange kinetics of epitaxial $PrBaCo_2O_{5+\delta}$ thin films," Applied Physics Letters **88**, 024103 (2006).
3. The Oxygen Non-stoichiometry and Electrical Conductivity of $La_{0.7}Sr_{0.3}Cu_{0.2}Fe_{0.8}O_{3-\delta}$, Chan Young Park, Frank V. Azzarello, and Allan J. Jacobson Journal of Materials Chemistry (2006), 16(36), 3624-3628.
4. Park, C. Y.; Huang, D. X.; Jacobson, A. J.; Hu, L.; Mims, C. A. Transport properties and phase stability of mixed conducting oxide membranes. Solid State Ionics (2006), 177(26-32), 2227-2233.
5. Kim, G.; Wang, S.; Jacobson, A. J.; Chen, C. L. Measurement of oxygen transport kinetics in epitaxial $La_2NiO_{4+d}$ thin films by electrical conductivity relaxation. Solid State Ionics (2006), 177(17-18), 1461-1467.
6. Kim, G.; Wang, S.; Jacobson, A. J.; Yuan, Z.; Chen, C. L., Impedance studies of dense polycrystalline thin films of $La_2NiO_{4+\delta}$ J. Mat. Chem. accepted

7. Kim, G.; Wang, S.; Jacobson, A. J.; Reimus, L.; Brodersen, P.; Mims, C.A., Rapid Oxygen Ion Diffusion and Surface Exchange Kinetics in the Oxides $LnBaCo_2O_{5+x}$ (Ln = Pr, Nd) with Perovskite Related Structures and Ordered A Cations. J. Mat. Chem. submitted.
8. Kim, G.; Jacobson, A. J., Electrochemical Characterization of $La_{2-x}Pr_xNiO_{4+x}$ for Application as Cathodes in Intermediate Temperature SOFCs, Mater. Res. Soc. Symp. Proc. submitted.

**9. Presentations**

1. "Evaluation of the Perovskite Related Oxides $Ln_2NiO_{4+\delta}$ (Ln =La, Pr) for Application as Cathodes in Intermediate Temperature SOFCs," G. Kim, S. Wang, and A. J. Jacobson, SECA Meeting, Boston, May 9-13, 2004.
2. "Fuel Cells," A. J. Jacobson at 'The Energy Advancement Leadership Conference', Reliant Center, Houston, TX, November 17 - 18, 2004.
3. "Applications of Mixed Conducting Oxides in Solid Oxide Fuel Cells and Ion Transport Membranes: Oxygen Non-stoichiometry and Oxygen Transport Kinetics." A. J. Jacobson, Department of Chemical Engineering, University of Houston, March 25, 2005.
4. "New Cathode Materials for Intermediate Temperature Solid Oxide Fuel Cells" A. J. Jacobson, C. A. Mims and Peter Reike, Sixth Annual SECA Workshop April 18-21, 2005.
5. "Evaluation of 214 Perovskite Related Oxides for Application as Cathodes in Intermediate Temperature SOFCs," G. Kim and A. J. Jacobson, Materials Research Society, Boston, November 29 to December 2, 2004.
6. "A Study of Oxygen Surface Exchange and Diffusion in $La_2NiO_{4+\delta}$ by Electrical Conductivity Relaxation." G. Kim and A.J. Jacobson, Electrochemical Society Meeting, San Antonio, May 9-13 2004.
7. "New Cathode Materials for Intermediate Temperature Solid Oxide Fuel Cells," A. J. Jacobson, C. A. Mims and Peter Reike, Pacific North West National Laboratory June 7 2005.
8. "Fast Oxygen Ion Diffusion and Surface Exchange Kinetics in the Oxides $LnBaCo_2O_{5+x}$ (Ln = Pr, Nd) with Perovskite Related Structures and Ordered A Cations," G. Kim, S. Wang, A. J. Jacobson, L. Reimus, P. Brodersen, C. A. Mims, Electrochem. Soc. Meeting, Los Angeles, Oct 16, 2005
9. "Oxygen Exchange Kinetics of $PrBaCo_2O_{5.5+\delta}$ Thin Films Prepared by Pulsed-Laser Deposition," G. Kim, S. Wang, A. J. Jacobson, Z. Yuan, W. Donner, C. L. Chen, L. Reimus, P. Brodersen, and C. A. Mims, Electrochem. Soc. Meeting, Los Angeles, Oct 16, 2005

10. “New Cathode Materials for Intermediate Temperature Solid Oxide Fuel Cells” A. J. Jacobson, C. A. Mims and Peter Reike, SECA CTP Peer Review Oct. 25-26, 2005 in Lakewood, CO.
11. “Electrochemical Characterization of $La_{2-x}Pr_xNiO_{4+x}$ for Application as Cathodes in Intermediate Temperature SOFCs,” G. Kim and A. J. Jacobson, MRS Meeting, Boston, Nov 27th 2006
12. “Double Perovskite PBCO Cathodes for Intermediate Temperature Solid Oxide Fuel Cells,” W. Gong, G. Kim, S. Wang, M. Yadav and A. J. Jacobson, MRS Meeting, Boston, Nov 27th 2006.